Henrik Viberg

Generation of Electromagnetic Emissions at Magnetic Reconnection Sites

Licentiate Thesis

UPPSALA
UNIVERSITET

Till Sara.
Vad vore jag
utan dina andetag

List of papers

This thesis is based on the following papers, which are referred to in the text by their Roman numerals.

I Mapping HF Waves in the Reconnection Diffusion Region

II Whistler Mode Waves at Magnetotail Dipolarization Fronts

Reprints were made with permission from the publishers.

Contents

1 The Space Environment ... 9
1.1 Looking Back ... 9
1.2 Plasma ... 10
1.2.1 Fields in a Plasma ... 11
1.2.2 Particle Motion ... 12
1.2.3 Plasma as a Fluid ... 13
1.2.4 Kinetic Description of a Plasma ... 14
1.3 The Solar Wind ... 16
1.4 Earth's Magnetosphere ... 17

2 The Cluster Spacecraft ... 19
2.1 Mission Overview ... 19

3 Magnetic Reconnection ... 23
3.1 Models for Reconnection ... 24
3.2 Observing Magnetic Reconnection ... 27

4 Waves in Space Plasmas ... 29
4.1 Plasma Wave Theory ... 29
4.1.1 Cold Plasma Approximation ... 30
4.1.2 Hot Plasma Dispersion Relation ... 32
4.1.3 Dispersion Surfaces ... 33
4.2 Observations ... 35
4.3 Waves in Reconnection ... 36

5 Into the Unknown ... 40
5.1 Magnetic Reconnection and High-Frequency Waves ... 40
5.2 Whistler Waves and Dipolarization Fronts ... 41
5.3 Outlook ... 42

6 Summary of papers ... 43

References ... 46

1. The Space Environment

> *"Begin at the beginning", the King said, gravely, "and go on till you come to an end; then stop."*
>
> – Lewis Carroll, *Alice in Wonderland*

1.1 Looking Back

The best known phenomenon in near-Earth space is probably the Northern lights, or *Aurora Borealis*. Records of these spectacular light displays date as far back as ancient China[26]. The northern lights have been an inspiration for various myths and legends through the ages. In Finnish, the northern lights are known as *revontulet*, fox fires, as it was believed that the lights came from fire foxes in Lapland as they ran across the mountains. Another legend comes from the south of Sweden: the swans migrating were competing to see who could reach farthest north. Some flew so far north that they got frozen into the ice and the beating of their wings caused the northern lights. Many other aboriginal people in the northern regions of the world believed the northern lights to be the souls of the dead, or omens of bad tidings[43].

It was not until the invention of accurate compasses that it was discovered that the northern lights occurred at the same time as large fluctuations in the magnetic field of the Earth. One of the first to show this was the Swedish scientist Anders Celsius and his contemporary Olof Petrus Hiorter[26].

Modern scientific inquiries into the nature of the northern lights include the works of, among many, the Norwegian physicist Kristian Birkeland. He concluded that that the northern lights are associated with currents, flowing along the magnetic field high up in the atmosphere. He also performed experiments where he placed a magnetized sphere called a *terella*, (Latin for 'little Earth') inside a vacuum vessel, and shot electron beams towards it. He then saw that this generated a glow near the poles of the sphere that were similar to the northern lights[26]. Some aurorae are the result of electrons travelling from space and down into the upper atmosphere, where they collide with the molecules in the air. The energy given to the electrons ultimately comes from the *solar wind*. In this thesis, we will discuss some mechanisms for converting energy in space plasmas. The mechanism responsible for energizing auroral electrons is a universal one, applicable to other space phenomena.

Figure 1.1. Left: An old Swedish legend says that swans got frozen to the ice in the north and their beating of the wings caused the northern lights. Drawing by Ingrid Sandahl, 1993. *Right:* Photo of the northern lights by Fredrik Broms.

1.2 Plasma

All the matter that surrounds us exists in different forms, or states. They can be either a gas like the air we breath, a liquid like water, or solid like ice. These are the states of matter we are accustomed to in our everyday life. But there is a fourth state of matter, which is not very common on Earth, but in the whole Cosmos it makes up about 99 % of all visible matter[4]. This state is called a *plasma* and consists of a gas of charged particles, such as protons and electrons. This may not seem as much of a difference from the gas state, you only swap the neutral atoms and molecules in a gas with electrically charged particles. But charged particles react to electric and magnetic fields, which their neutral counterparts do not. Also, the particles in the plasma can, in turn, generate electric and magnetic fields. This is called *collective* behaviour. The interaction between particles and electromagnetic fields is much stronger than the effects of collisions between the particles, unlike a neutral gas where the motion of a particle is determined by collisions with its neighbours.

A plasma is, despite being composed of charged particles, neutral on average from an outside point of view. This is called *quasineutrality*. The spatial distance over which quasineutrality holds is determined by how efficient the plasma is at shielding charge differences. If there is a positive charge in the plasma, it will attract electrons and repel ions, resulting in a cloud of electrons that shields the positive charge[26]. The opposite of course holds for a negative charge. The potential from a single point charge in a vacuum is

$$\phi = \frac{q}{4\pi\varepsilon_0 r}, \tag{1.1}$$

where q is the charge of the particle, r is the distance from it, and ε_0 is the permittivity of free space. In a plasma, the potential from the particle will be affected by the other charged particles. If the particle is an ion, electrons will attract to it and shield the potential at distances far from the particle:

$$\phi = \frac{q}{4\pi\varepsilon_0 r} e^{-r/\lambda_D}, \tag{1.2}$$

where λ_D is the *Debye length*, defined as

$$\lambda_D = \sqrt{\frac{\varepsilon_0 k_B T_e}{nq^2}}, \tag{1.3}$$

where k_B is Boltzmann's constant, n is the electron density, and T_e is the electron temperature. From the expression for the Debye length, it is clear that a hot plasma has a longer Debye length and thus the system must be larger to still be considered quasineutral. Also, a denser plasma has a shorter Debye length than a more tenuous one. To summarize: the definition of a plasma is a gas of charged particles, that is on average neutral, and that exhibits collective behaviour.

1.2.1 Fields in a Plasma

A plasma is affected by electromagnetic fields, governed by Maxwell's equations[26]:

$$\nabla \cdot \mathbf{E} = \frac{\rho_c}{\varepsilon_0}, \tag{1.4}$$

$$\nabla \times \mathbf{E} = -\frac{\partial \mathbf{B}}{\partial t}, \tag{1.5}$$

$$\nabla \cdot \mathbf{B} = 0, \tag{1.6}$$

$$\nabla \times \mathbf{B} = \mu_0 \mathbf{J} + \mu_0 \varepsilon_0 \frac{\partial \mathbf{E}}{\partial t}. \tag{1.7}$$

The quantities $\mathbf{E}$ and $\mathbf{B}$ are the electric and magnetic field, respectively. $\mathbf{J}$ is the total current density, and ρ_c is the total charge density. The constants ε_0 and μ_0 are the permittivity and permeability of free space, respectively.

The large-scale magnetic fields in a space plasma are generated inside a celestial body, e.g. the Sun or the Earth by a dynamo process by moving charges in the interiors of these bodies[7]. For the case of the Sun, the moving charges is plasma in the solar interior, whereas for Earth the magnetic field is generated by the conducting liquid iron in Earth's outer core. These fields are not stable over a large time period. The Sun's magnetic field, for example, changes polarity about every 11 years and its configuration varies from almost completely dipolar to toroidal over the course of such a solar cycle. Also the Earth's magnetic field has undergone pole shifts several times during the lifetime of the planet.

1.2.2 Particle Motion

To determine how the electromagnetic fields determine the motion of charged particles, we need some more equations. First, the motion of a single charged particle in an electric and a magnetic field is governed by the Lorentz force:

$$\mathbf{F} = q(\mathbf{E} + \mathbf{v} \times \mathbf{B}) = m\mathbf{a}, \tag{1.8}$$

in which $\mathbf{v}$ is the particle velocity and $\mathbf{a}$ is its acceleration due to the force $\mathbf{F}$. This equation shows that the force on a charged particle is in the same direction as the electric field, and perpendicular to both the particle's velocity and the magnetic field. To analyze a particle's motion due to the Lorentz force, one can look at a simplified situation, where there is no applied electric field. In this setup, there is only the contribution from the $\mathbf{v} \times \mathbf{B}$-term. Re-writing the equation using time derivatives gives the two equations

$$\frac{\partial v_x}{\partial t} = \frac{qB}{m} v_y, \tag{1.9}$$

$$\frac{\partial v_y}{\partial t} = -\frac{qB}{m} v_x, \tag{1.10}$$

which has the solutions

$$x = r_c \cos \omega_c t + x_0, \tag{1.11}$$

$$y = r_c \sin \omega_c t + y_0, \tag{1.12}$$

where

$$\omega_c = \frac{qB}{m} \tag{1.13}$$

is the gyrofrequency of the particle, determined by the strength of the magnetic field and the charge and mass of the particle. r_c is the gyroradius, determined by

$$r_c = \frac{v_\perp}{|\omega_c|}. \tag{1.14}$$

Thus the Lorentz force causes the particles to gyrate around the magnetic field, with frequency determined by (1.13), see Figure 1.2.

A uniform electric field will modify the motion and introduce a drift velocity in the direction perpendicular to both $\mathbf{E}$ and $\mathbf{B}$:

$$\mathbf{v}_E = \frac{\mathbf{E} \times \mathbf{B}}{B^2}. \tag{1.15}$$

As can be seen in this equation, the drift velocity is independent on particle mass and charge, so both negative and positive charges will drift in the same direction and with the same speed. Thus, the $\mathbf{E} \times \mathbf{B}$ drift does not introduce a current. There are other drift velocities as well, determined by e.g. the gradient and the curvature of the magnetic field[26].

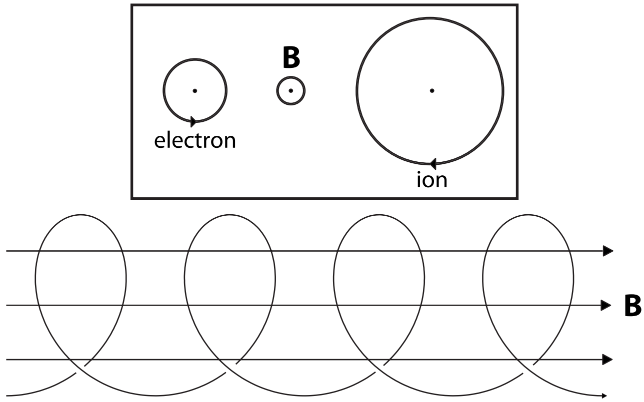

Figure 1.2. Particle motions in a uniform magnetic field. Top: directions of gyration; right-handed (electrons) and left-handed (ions). Bottom: helical orbit of an electron with a velocity component parallel to the magnetic field.

1.2.3 Plasma as a Fluid

It is possible to describe a plasma by calculating each particle's motion individually. But since a plasma volume may contain perhaps 1000 particles per cubic centimeter, and the spatial scale of the plasma of interest may be 1000s of km, the total number of particles will be huge. Thus, this approach is best left to very powerful computers. Instead, one may treat the plasma as a fluid, just like ordinary gases can be in fluid dynamics, if one adds the effects of the electric and magnetic fields. A plasma in the fluid description has to obey conservation laws. The first of these is the *continuity equation*[4,26]:

$$\frac{\partial n}{\partial t} = \nabla \cdot (n\mathbf{v}) = 0, \tag{1.16}$$

which states that the number density of particles in a given volume is conserved during the fluid motion, if there are no sources or sinks on the right-hand side. The momentum density of the fluid must also be conserved, as is described by the *momentum equation*[4,26]:

$$m\left(\frac{\partial \mathbf{v}}{\partial t} + \mathbf{v}\cdot\nabla\mathbf{v}\right) = q\,(\mathbf{E} + \mathbf{v}\times\mathbf{B}) - \nabla\cdot\mathsf{P}. \tag{1.17}$$

This is actually the Navier-Stokes equation with a Lorentz force term added[4]. The $\nabla\cdot\mathsf{P}$ term is the contribution from the fluid pressure and viscosity. The momentum equation introduces a second-order term P, which must also be described by another equation, which in turn introduces a third-order term, and so on, forming a never ending hierarchy of increasingly higher-order terms. Thus, in order to solve the equations, they must truncated at some level. One way of doing this is to keep only the continuity and momentum equations and then introduce an *equation of state*, which describes the plasma pressure. The simplest form is that describing a plasma with an isotropic pressure

$$\mathsf{P} = \begin{pmatrix} p & 0 & 0 \\ 0 & p & 0 \\ 0 & 0 & p \end{pmatrix}. \tag{1.18}$$

For an isothermal plasma the pressure p is

$$p = nk_BT, \tag{1.19}$$

and for an adiabatic plasma

$$p = p_0 \left(\frac{n}{n_0}\right)^{\gamma}. \tag{1.20}$$

1.2.4 Kinetic Description of a Plasma

The many-particle and fluid descriptions are the two extreme description of a plasma; in the many-particle description, one takes into account the motion of each individual particle, and the microscopic electromagnetic fields generated by this motion. In the fluid description, one treats the entire plasma as a fluid with just on velocity and consider only the macroscopic fields. The former approach is the most accurate, of course, but requires a lot of computational power even for relatively few particles. The latter approach is computationally preferable, but not always sufficiently accurate.

There exists, however, a middle road to this problem. One can take advantage of the collective behaviour of the plasma and look at the statistical properties of it. This is the idea behind the *kinetic* description of a plasma. The core of kinetic theory is the *distribution function*, $f = f(\mathbf{v}, \mathbf{x}, t)$, which gives the *probability* of finding a particle at a certain velocity $\mathbf{v}$ and position $\mathbf{x}$ at time t [26]. The vector space spanned by the six independent vectors in $\mathbf{x}$ and $\mathbf{v}$ is called *phase-space*. In practical applications, one is most often interested in how the distribution depends on the velocity, at a given point in space and at a certain time, hence one wants to determine $f = f(\mathbf{v})$. The distribution function for a plasma in thermal equilibrium is called a *Maxwellian* distribution, and in one dimension, it has the form

$$f(v) = n\left(\frac{m}{\pi v_{th}^2}\right)^{\frac{3}{2}} e^{-\left(\frac{v}{v_{th}}\right)^2}, \tag{1.21}$$

where v_{th} is the electron thermal speed

$$v_{th} = \sqrt{\frac{k_BT_e}{m_e}}. \tag{1.22}$$

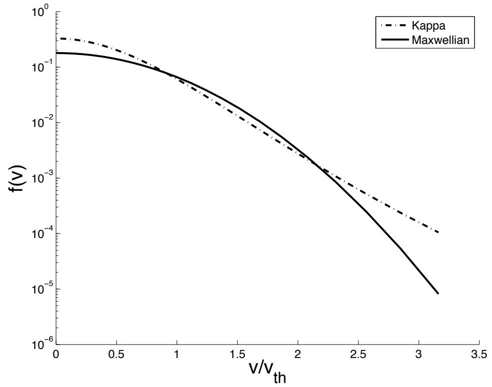

Figure 1.3. Maxwellian (solid) and kappa (dashed) distribution. Vertical axis is in log-scale.

Another distribution, and one that occurs often in space plasmas, is the *kappa distribution*[4]. It decreases as a power law instead of an exponential, so at high velocities, it exhibits a 'tail'. Figure 1.3 shows the difference between a kappa and a Maxwellian distribution. One may describe a plasma using several distribution functions, e.g. one for each particle species. From the distribution function, the number density can be calculated by integrating over velocity space:

$$n = \int\limits_{\mathbf{v}} f(\mathbf{v}) d\mathbf{v}. \tag{1.23}$$

The average, or bulk, velocity is obtained by calculating the first-order moment:

$$\mathbf{V} = \frac{1}{n} \int\limits_{\mathbf{v}} \mathbf{v} f(\mathbf{v}) d\mathbf{v}, \tag{1.24}$$

where $\mathbf{v}'$ is used for the integration variable. In the same manner as above, the pressure tensor P and higher-order moments can be derived. The total charge and current densities are given by

$$\rho = \sum_s q_s n_s, \tag{1.25}$$

$$\mathbf{J} = \sum_s q_s n_s \mathbf{V}_s, \tag{1.26}$$

where s denotes the individual particle species. The distribution function obeys a conservation equation in phase-space, the *Boltzmann equation:*

$$\frac{\partial f}{\partial t} + \nabla \cdot (n\mathbf{v}) + \frac{q}{m} (\mathbf{E} + \mathbf{v} \times \mathbf{B}) \cdot \nabla_{\mathbf{v}} f = \left(\frac{\partial f}{\partial t} \right)_c . \tag{1.27}$$

The first two terms describe the change of f with respect to time as one moves along with the plasma (the convective derivative). The third term is the contribution from the Lorentz force times the velocity-space gradient of f. The term on the right-hand side of (1.27) describes the change of f due to collisions. In many space plasma applications, the plasma may be assumed to be collisionless, and the collision term vanishes, giving the *Vlasov equation*[45]

$$\frac{\partial f}{\partial t} + \nabla\cdot(n\mathbf{v}) + \frac{q}{m}(\mathbf{E}+\mathbf{v}\times\mathbf{B})\cdot\nabla_{\mathbf{v}}f = 0 \tag{1.28}$$

One can of course replace the Lorentz force with a more general expression for the forces acting on the plasma, but for most cases, the above expression is sufficient.

1.3 The Solar Wind

The Sun is a giant ball of hot plasma held together by its gravity. The energy the Sun radiates into space has its origin in the very core of the star. There, hydrogen ions have enough energy to overcome their mutual repulsion and fuse together, creating helium and releasing energy[7]. The visible light from the Sun is not all that it gives off to space. Electromagnetic radiation in all frequencies from the extreme long wavelength radio waves to energetic gamma rays is observed. In addition to this, there exists a continuous stream of particles flowing out from the Sun. This is the *solar wind*, travelling from the Sun and out into the solar system at high speeds.

The main components of the solar wind are electrons and ions of hydrogen and helium. The speed of the solar wind varies, but a common value is around 500 km/s at the orbit of the Earth, taking 3-4 days to reach the orbit of the Earth[4]. The speed of the solar wind is not that high in the solar atmosphere. Instead, it is accelerated in a region above the Sun called the *corona*. This is the part that can be seen during a solar eclipse. The corona is very hot, with temperatures of more than one million Kelvin.

We will now discuss what happens to the Sun's magnetic field as the solar wind travels away from the Sun. The current in a plasma is determined by Ohm's law:

$$\mathbf{J} = \sigma(\mathbf{E}+\mathbf{v}\times\mathbf{B})\,. \tag{1.29}$$

By combining Faraday's (1.5), Ampére's (1.7) and Ohm's (1.29) laws, we get the equation (neglecting the $\partial\mathbf{E}/\partial t$ term in Ampére's law, which is okay for non-relativistic velocities):

$$\frac{\partial\mathbf{B}}{\partial t} = \frac{1}{\mu_0\sigma}\nabla^2\mathbf{B} + \nabla\times(\mathbf{v}\times\mathbf{B})\,. \tag{1.30}$$

This equation describes the evolution of the magnetic field due to motion of the plasma (second term on the right-hand side) and diffusion (first term). The parameter σ denotes the conductivity. If the conductivity is very low, the first term will dominate and we get a simple diffusion equation

$$\frac{\partial B}{\partial t} = \frac{1}{\mu_0 \sigma} \nabla^2 \mathbf{B}, \tag{1.31}$$

with a diffusion time

$$\tau_D = \mu_0 \sigma L^2, \tag{1.32}$$

where L is the characteristic length of the system. Typical values of the solar wind conductivity are very high, leading to a long diffusion time; during the 4 day journey from the Sun to the Earth, the plasma will have diffused only about 1000 m[4].

The other extreme of (1.30) gives

$$\frac{\partial \mathbf{B}}{\partial t} = \nabla \times (\mathbf{v} \times \mathbf{B}), \tag{1.33}$$

which states that the magnetic field moves with the plasma, and that the magnetic flux through a surface of a plasma volume is constant, even if the fluid elements of the plasma move relative each other. This is called the *frozen-in* condition. Since the conductivity of the solar wind is very high, the induction equation will reduce to (1.33) and the solar wind will drag the Sun's magnetic field with it as it moves out into the solar system. This magnetic field is called the *interplanetary magnetic field*, IMF.

1.4 Earth's Magnetosphere

The Earth's magnetic field acts as an obstacle for the solar wind. The frozen-in condition requires that the solar wind plasma is deflected around the Earth, and the region in space where the Earth's magnetic field dominates the plasma dynamics is called the *magnetosphere*[26]. In a vacuum, the magnetic field of the Earth would roughly have the shape of a dipole, but due to the solar wind, it will get a more complex shape. In front of the Earth, the momentum of the solar wind presses the field lines together, and on the side facing away from the Sun, the field is stretched out.

Figure 1.4 shows a sketch of the magnetosphere and its regions. The first region from the left is the *bow shock*, which forms because the solar wind speed is supersonic and thus shocks will form whenever it encounters an obstacle (for a more detailed discussion, see e.g. Baumjohann and Treumann[4]). Behind the bow shock lies the *magnetosheath*, and here the plasma flow is subsonic. The boundary between the solar wind and magnetosphere plasmas is called the *magnetopause*, and here the total solar wind pressure is balanced by the magnetospheric pressure. The distance to the magnetopause can be approximated by calculating these pressures. The sub-solar magnetopause is at a distance of about 10 R_E[38].

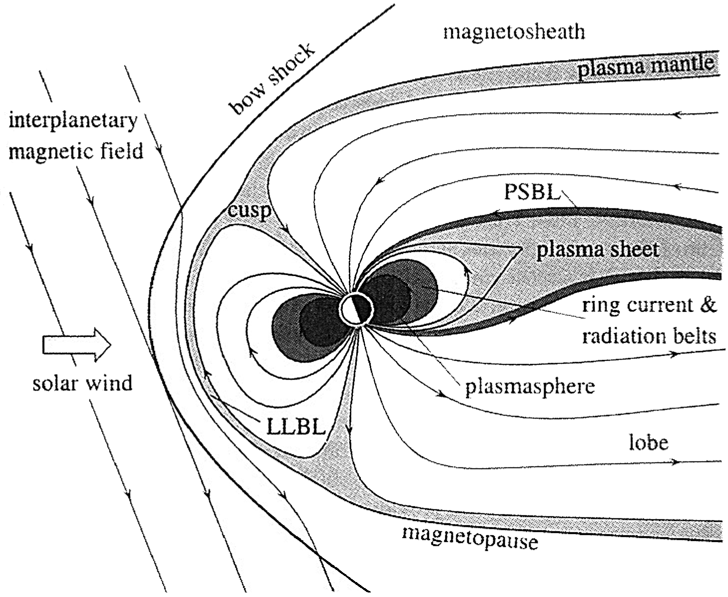

Figure 1.4. Sketch of the Earth's magnetosphere with the different regions and currents labelled Figure adapted from[38].

The part of the magnetosphere extending away from the direction of the Sum is called the *magnetotail*. It can be divided into the *tail lobes*, and the *plasma sheet*. The lobes have a low plasma density and temperature. The plasma sheet lies inside the tail lobes and here a cross-tail current flows. This current is the result of the oppositely directed magnetic field in the plasma sheet. There are also currents flowing along the surface of the magnetopause. Closer to Earth, we find the *plasmasphere*, a region consisting of cold, dense plasma. Inside the plasmasphere one finds two belts of highly energetic plasma called the *Van Allen radiation belts*.

The *polar cusp* is the region where Earth's magnetic field changes direction so that plasma may flow along the field lines and down from the magnetosheath to the *ionosphere*. The ionosphere is a region of the Earth's atmosphere where solar UV radiation ionizes parts of the neutral gas. Space is considered to begin at 80-100 km altitude, and the ionosphere extends down to about 80 km. Closer to Earth than that, there are to much collisions that ions and electrons recombine[4]. The ionosphere is the only region in the magnetosphere where the plasma cannot be considered collisionless.

2. The Cluster Spacecraft

It's a magical world, Hobbes, ol' buddy... Let's go exploring!
– Calvin, *Calvin & Hobbes*

Ever since the dawn of the Space Age have scientists investigated the space environment using an armada of spacecraft or ground based instruments of different design and sophistication. A full review of spacecraft and Earth-based missions would fill several books, so in this chapter we will only describe the Cluster spacecraft, from which the data presented in our papers come from.

The Cluster mission was first proposed in the early 1980's, when ESA, the European Space Agency, called for designs of a European satellite that would investigate the Earth's magnetosphere. One and a half decade later, the four Cluster satellites were set to launch from Kourou in French Guiana. But shortly after launch, the Ariane 5 rocket carrying the satellites exploded and the satellites were lost.

Instead of giving up on the spot, ESA and the collaborating research institutes that built the various instruments buckled down and rebuilt the satellites. In the summer of 2000, the new mission, called *Cluster II* but most often just *Cluster*, was launched pair-wise into orbit by Russian Soyuz rockets. This time, the launch was successful, and the four spacecraft entered their polar orbit to begin exploring our cosmic backyard.

2.1 Mission Overview

The four Cluster spacecraft was inserted into in a tetrahedron shaped configuration, in a polar orbit with a perigee of 19 000 km, apogee of 119 000 km, and an orbital period of 57 hours. However, the orbit of the spacecraft has been changed several times during the mission. It is necessary to use four spacecraft to be able to distinguish between spatial and temporal variations in the plasma. With four spacecraft, three-dimensional structures can be resolved. The spatial scales of magnetospheric phenomena varies greatly, and so must the spatial configuration of the Cluster spacecraft. The separation between the satellites can be as small as a few km, and as large as 10000 km, depending on the mission phase.

Each Cluster satellite carries an identical set of 11 different instruments, designed and constructed by researchers in Europe and the USA. Together, the instruments measure the space environment of the magnetosphere and the solar wind.

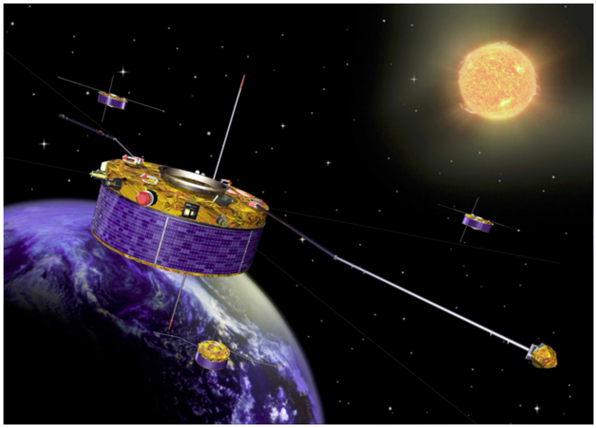

Figure 2.1. The Cluster spacecraft armada. Source: *http://sci.esa.int/cluster/*

Electric and Magnetic Field Measurements
The electric fields are measured by the *EFW* (Electric Field and Wave) instrument[23]. EFW consists of four Langmuir probes on 44 meter long wire booms extending from the spacecraft. Two opposite probes form a dipole antenna in the spin plane. By measuring the probe potential and dividing by the probe-to-probe distance, one obtains a measure of the electric field between the probes. The spacecraft spins with a period of about 4 seconds, so the measurements are in the spacecraft coordinate system, but is also delivered in GSE (geocentric solar ecliptic) coordinates. The probes all lie in the spin plane of the spacecraft, so only the 2D electric field is measured. The third component is obtained by assuming that $\mathbf{E}\cdot\mathbf{B} = 0$. This procedure works well as long as the magnetic field has an angle of at least 15° and $|B_z| \geq 2$ nT[28]. The sample rate for the electric field measurements is either 25 Hz (normal mode, NM), or 450 Hz (burst mode, BM). In addition to this, the instrument can measure short sequences at 36 kHz. The spacecraft potential is obtained by averaging the probe-to-spacecraft potentials for the individual probes, with a time resolution of 0.2 seconds.

The *WBD* (Wide Band Data) instrument provides high time resolution wave form data of the electric or magnetic field[22]. WBD can deliver data with a sampling frequency of up to 220 kHz, but the trade-off is that it only measures in one direction at a time. This can be along either of the two dipole antennas or from two of the magnetic field search coils, one of which has its axis is in the spin plane, and the other along the spin axis. Also, due to the high sample rate, the data volume will be very large, exceeding the capacity of the onboard memory. The data must therefore be transmitted directly to a ground station. This limits the WBD coverage considerably, so only about 4 % of the is there WBD data available.

Name	Description	Country
ASPOC	Controls the spacecraft potential[41].	Austria
CIS	Ion spectrometer measuring the composition, mass and distribution of ions[39].	France
DWP	Controls the Cluster wave instruments (EFW, STAFF, WBD, and WHISPER)[52].	UK
EDI	Probes the electric field by firing beams of electrons and measuring the time it takes for them to return[37].	USA
EFW	Measures the electric field and also density, via the spacecraft potential[23].	Sweden
FGM	Measures the DC magnetic field using fluxgate magnetometers[2].	UK
PEACE	Instrument for measuring the electron distribution[35].	UK
RAPID	Measures the high energy electrons and ions[51].	Germany
STAFF	Used to measure the AC magnetic and electric field[9].	France
WBD	Delivers high-resolution data for electric and magnetic fields[22].	USA
WHISPER	Resonance sounder that measures the electron density and high-frequency waves[10].	France

Table 2.1. *The different Cluster instruments. From Escoubet, et al.*[17]

The DC magnetic field is measured by the *FGM* (FluxGate Magnetometer) instrument[2]. It consists of two tri-axial fluxgate magnetometers, and has a measurement range of up to about $\pm 65\ \mu$T. The wave power is attenuated at frequencies higher than 10 Hz. The data is most commonly delivered at 22.4 and 67.2 Hz (burst mode 2 and 1, respectively).

The AC magnetic field is measured using a search coil magnetometer by the *STAFF* (Spatio-Temporal Analysis of Field Fluctuation) instrument[9]. STAFF provides the magnetic field waveform (sampled at either 25 or 450 Hz) and the spectral matrix. The spectral matrix is calculated using the 3D magnetic field and 2D electric field (from EFW). From the spectral matrices, the polarization parameters, propagation directions and energy flux of the waves can be obtained. The time resolution for the spectral matrices is 4 seconds in normal mode, and 1 second in burst mode. The frequency range in normal mode is 8 Hz to 4 kHz, while in burst mode it is 64 Hz to 4 kHz. STAFF also uses EFW electric field measurements for calculating the spectral matrices.

The *EDI* instrument measures the electric field by firing beams of electrons into space and measuring the time it takes for them to return[37]. From EDI data one can get the electric field component along the spacecraft spin axis, unlike for EFW where it is estimated. EDI also makes measurements of the electron count, but only for a narrow energy range and pitch angle.

Particles

The *CIS* instrument measures the composition and distribution of the ions in the space plasma[39]. CIS consists of two parts; HIA (Hot Ion Analyzer) for measuring the full ion distribution function in 3D, and CODIF (Composition and Distribution Function analyser) that uses a time-of-flight analysis to measure ion velocities. CIS can measure ions with energies up to 32 keV per unit charge, while CODIF measures ions up to an energy of 40 keV per unit charge. On the C2 satellite, the CIS instrument is not operational.

For measuring electrons, the *PEACE* instrument can be used[35]. It has two sensors, one for low energy and one for high energy electrons that measure the electron distribution in the range of 0.6 eV to about 26.5 keV. From the distribution, electron moments such as density and velocity are calculated by the onboard electronics. The high energy ($\gtrsim$ 30 keV) electrons are measured by the *RAPID* instrument[51].

3. Magnetic Reconnection

There's something that doesn't make sense. Let's go and poke it with a stick.

– The Doctor

Magnetic reconnection is a process in plasma physics whereby magnetic energy is converted into kinetic energy and heat of the plasma. It is a very powerful process, responsible for e.g. solar flares and the onset of magnetospheric substorms. The energy release requires a change in magnetic topology, otherwise the different plasma domains of, for example, the solar wind and the magnetosphere would not become interconnected and not allow plasma from the solar wind to enter the magnetosphere. For this change in topology to happen, the frozen-in flux condition must be broken[6].

If the interplanetary magnetic field, IMF, has a southward component, the frozen-in flux may be locally broken, and allow merging of the magnetic fields. This is illustrated in Figure 3.1. The field line from the Earth is split into two lines (labelled (2) in the figure), both connected to the IMF. These are then convected around the Earth and into the nightside magnetosphere, where the lines will meet and reconnect (label (7)). The reconnected field line is now very stretched out and thus has a lot of magnetic tension. Dayside (magnetopause) and nightside (magnetotail) reconnection is quite different from each other. At the magnetopause, it is mostly kinetic energy of the solar wind that is converted and stored as magnetic energy, whereas in the magnetotail, the stored magnetic energy is released, and rather rapidly so, and accelerates and heats the plasma[38].

The field lines merge and reconnect along a line called the *X-line* (due to it resembling the letter X in two-dimensions). For magnetotail reconnection, the X-line is typically located at 20-30 R_E from the Earth[38]. As the newly reconnected field line relaxes its magnetic tension and convects the plasma towards the Earth. There is also plasma flow away from the Earth, but we will not discuss that here. As the flow of plasma moves towards the Earth, it encounters the dense plasma sheet (see Figure 1.4) and the magnetic field lines will become compressed, forming a *flux pile-up region* and a *dipolarization front*, which is identified as a sharp gradient in the z-component of the magnetic field and associated with fast plasma flows and energetic particles. We will discuss dipolarization fronts more in Chapter 5.

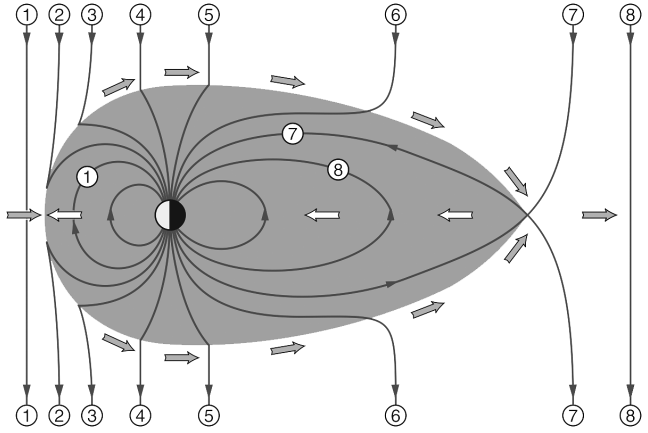

Figure 3.1. View of magnetic reconnection in the magnetosphere during southward IMF. From [4].

3.1 Models for Reconnection

The concept of magnetic reconnection has been debated since the 1950's, when Dungey came up with the idea of field-line reconnection [13]. Several models of reconnection has been put forth. Here we will briefly discuss three of these, the *Sweet-Parker*, *Petschek*, and Hall models.

Sweet-Parker Reconnection

The Sweet-Parker model [46,36] is based on a quasi-stationary situation with two regions of oppositely directed magnetic fields collide. Because of the opposite magnetic fields, a current sheet must exist. Far from this current sheet, the conductivity is high and the frozen-in condition holds. In the current sheet however, the conductivity is low, and the magnetic fields on each sides are allowed to diffuse. The *diffusion region* in the Sweet-Parker model is considered thin, with length $2L$, thickness $2l$, and $L \gg l$, as seen in Figure 3.2. Due to conservation of magnetic flux, conservation of mass, and pressure equilibrium, the speed at which the plasma is ejected from the diffusion region (the *outflow speed*) is [38]

$$v_{out} = \frac{B_{in}}{\sqrt{\mu_0 \rho}} = v_{Ai}, \tag{3.1}$$

where B_{in} is the magnetic field far from the diffusion region, $\rho = n_i m_i$ is the ion mass density, and v_{Ai} is the *Alfvén speed* in the inflow region. The *reconnection rate* in the Sweet-Parker model is

$$M_{SP} = \frac{1}{\sqrt{S}}, \tag{3.2}$$

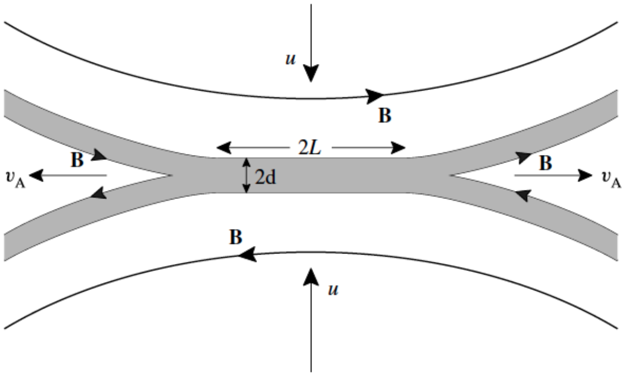

Figure 3.2. The Sweet-Parker reconnection configuration. From[7].

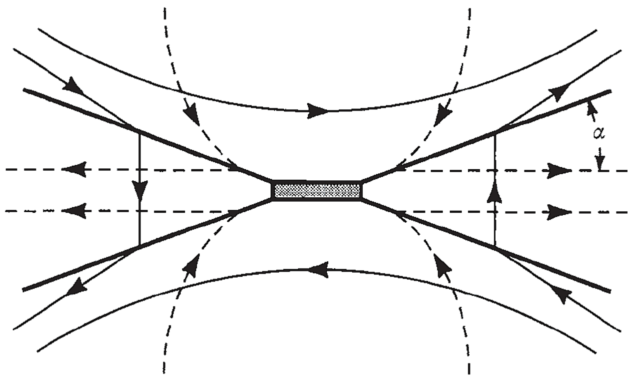

Figure 3.3. Petschek's reconnection model. From[6].

where $S = \frac{Lv_A}{\eta}$ is the *Lundqvist number*, or *magnetic Reynolds number*. This reconnection rate is very small, too small to account for the fast reconnection rates required to understand e.g. solar flares.

Petschek Reconnection

In the Sweet-Parker model, the reconnection rate is proportional to $L^{-1/2}$, so the smaller the length of the diffusion region, the higher the reconnection rate. Since in that model L is large, the reconnection rate is slow. Petschek made the suggestion that the Sweet-Parker diffusion region was limited to a small region of the boundary between the opposing magnetic fields. Thus the reconnection could proceed at a higher rate[38]. In Petschek's model, the magnetic fields would meet at the small diffusion region, with standing shock waves extending from the diffusion region, see Figure 3.3. These shocks serve to accelerate and heat the plasma, so that the conversion of magnetic energy is not restricted to

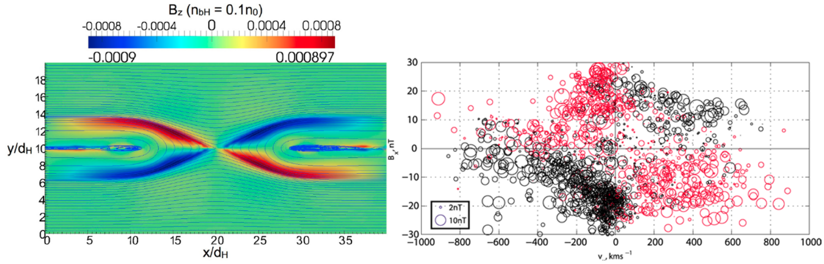

Figure 3.4. Left: A simulation result showing the Hall magnetic field. Note that here the coordinate system is different, with the B_z being the out-of-plane component of the magnetic field. Figure is from[29]. *Right:* A scatter plot of several measurements of B_y versus v_x and B_x. Black symbolizes $B_y > 0$ and red $B_y < 0$. The radii of the circles gives the magnitude of B_y. Figure is from[15].

just the diffusion region. The maximum reconnection rate in Petschek's model is[38]

$$M_P = \frac{\pi}{8 \log S}, \tag{3.3}$$

where S is defined as $S = \frac{L_e v_A}{\eta}$, L_e being the scale of the external region in Petschek's configuration. This reconnection rate matches rather closely the rates observed for flares. This made Petschek's model the standard for magnetic reconnection for several years. However, Biskamp[6] mentions numerical simulations showing that the diffusion region becomes larger for increasing reconnection rate, contrary to Petschek's model, and that no shock structure is formed. Biskamp argues that this is not a result of poorly chosen boundary conditions in the simulations, but of the physics of the current sheet. A reconnection geometry similar to Petschek's can be achieved, however, if one introduces an enhanced resistivity (called *anomalous resistivity*) in the diffusion region. Although Petschek's model is not self-consistent, it is still useful as a conceptual picture for reconnection.

Hall Reconnection

Observations have shown that the diffusion region is actually made up of an ion diffusion region and an electron diffusion region, the latter being smaller than the former. The ion diffusion region is where the frozen-in condition for the ions is broken and they become unmagnetized. The scale of the ion diffusion region is of the order of the *ion inertial length*, which is $lambda_i = c/\omega_{pi}$[14]. The electrons remain frozen into the field, until they too are demagnetized in the electron diffusion region, which is on the scale of the *electron inertial length.* This separation of ions and electrons is caused by the Hall term in the generalized Ohm's law and creates currents in the plane of the reconnection geometry, which in turn create an out of plane, quadrupolar, magnetic field called the *Hall field*. Figure 3.4 shows both a simulation and

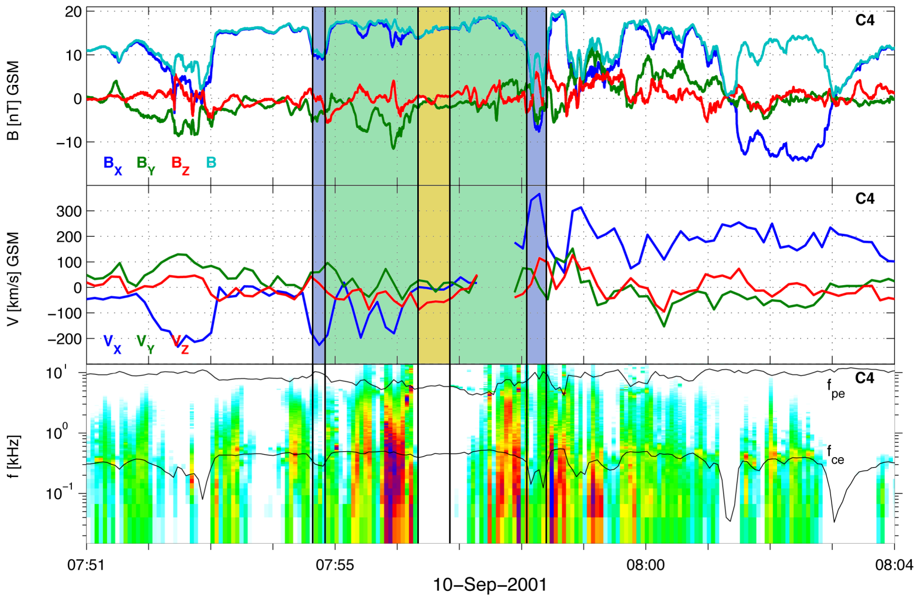

Figure 3.5. Cluster data of a reconnection region crossing. The top panel shows the magnetic field and the lower panel the ion velocities, both in GSM coordinates. The z-component of the magnetic field changes signs between 07:55 and 07:58, as does B_y. In the same period of time, v_x reverses sign from negative (tailward) to positive (Earthward) flow. B_x stays positive during the whole time. Thus the Cluster spacecraft moves Earthward and stays above the current sheet. The reversal of the direction of B_y shows the presence of the Hall field. The colored regions represent; blue: outflow; green: separatrix; yellow: inflow region. The bottom panel is the spectrum of the WBD electric field measurements. The most intense electric field activity is within the separatrix regions. Figure adapted from[50].

an observation of the Hall field. It has been shown in simulations[5] that any model that includes the Hall term leads to roughly the same reconnection rate, regardless of the actual mechanism for the breaking of field lines.

3.2 Observing Magnetic Reconnection

The conceptual picture of reconnection in Figure 3.3 tells us what to look for when trying to find evidence of magnetic reconnection from spacecraft data. Depending on how the spacecraft trajectory is with respect to the reconnection region (it is actually the reconnection region that moves across the spacecraft, since the spacecraft velocity is low compared to those of the plasma), we expect different signatures in the data. Consider, for example, a trajectory crossing northward (i.e. positive z-coordinate in the GSM system) of the X-line and towards the Earth. According to Figure 3.3, the spacecraft should first observe ion flow in the negative x-direction and a positive value of B_x and B_z. As it leaves this *ion outflow region*, it encounters the *separatrix region*, characterized by strong parallel electric fields. The separatrix region is located between the outflow jet and the magnetic *separatrix*[40], which is defined as the last reconnected field line. The spacecraft then enters the rather quiet *inflow region*, where the magnetic field is dominated by its x-component. After passing above the diffusion region, it will cross the other separatrix region, and then the Earthward outflow region. Here it starts to observe a positively directed ion flow, a still positive B_x, and a negative B_z. The y-component of the magnetic field (the Hall field) should change from positive to negative during this excursion. Of course, spacecraft may traverse the reconnection region in any direction, making the identification of it more difficult. Figure 3.5 shows an example of a reconnection region encounter with the magnetic field (FGM) in the first panel, the ion velocity (CIS) in the second, and the electric field spectrum (WBD) in the third panel. The blue regions are the outflow regions, the green the separatrix regions, and the yellow is the inflow region. In this case, the spacecraft encounters these three regions several times. This figure is adapted from Paper I.

4. Waves in Space Plasmas

Nothing shocks me. I'm a scientist.

– Harrison Ford, *Indiana Jones*

A wave is a disturbance travelling in a medium and transferring energy[53]. In our everyday life we encounter waves in the air, as sound waves, in the water as surface waves, and even rely on light waves for our vision. Waves transport energy without any transport of mass. In a plasma, there can exists a large variety of waves, though not infinitely many. The wave types, or modes, that can exist in a plasma depends on the properties of the plasma itself. Waves are very important in plasma physics, as they allow for the transport of energy from one part to another, and can reorganize the plasma configuration and accelerate particles[45].

A wave has a *frequency* ω (rad/s), and a *wave number/vector* $\mathbf{k}$ m^{-1}. The *phase velocity*, which is the velocity of wave propagation, is defined as

$$\mathbf{v}_{ph} = \frac{\omega}{\mathbf{k}}, \tag{4.1}$$

and the *group velocity*, which is the velocity of energy flow, is defined as

$$\mathbf{v}_g = \frac{\partial \omega}{\partial \mathbf{k}}. \tag{4.2}$$

In this chapter, we shall derive a wave equation using Maxwell's equations and Ohm's law and later derive the general *dispersion relation* for waves in a plasma. The dispersion relation tells how a wave's frequency relates to its wavenumber. From the general dispersion relation, specific solutions corresponding to different wave modes are then given. How one can observe waves in space is also discussed.

4.1 Plasma Wave Theory

To derive the general wave equation, one starts with Faraday's (1.5) and Ampère's (1.7) equations and then take the curl of the first and the time derivative of the second, and combine, using $\nabla \times (\nabla \times \mathbf{E}) = \nabla(\nabla \cdot \mathbf{E}) - \nabla^2 \mathbf{E}$, to get

$$\nabla^2 \mathbf{E}_1 - \nabla(\nabla \cdot \mathbf{E}_1) = \mu_0 \frac{\partial \mathbf{J}_1}{\partial t} + \mu_0 \varepsilon_0 \frac{\partial^2 \mathbf{E}_1}{\partial t^2}. \tag{4.3}$$

This is the *general wave equation*. The subscript 1 in (4.3) comes from the linearization $X = X_0 + X_1$, where X_0 denotes the equilibrium quantity and X_1 the perturbation. For both the electric field and the current, the zeroth-order term is zero. This equation is quite formidable, but luckily, one may approximate the electric field as *plane waves*:

$$\mathbf{E}_1 = E_1^0 e^{i(\mathbf{kr}-\omega t)}, \tag{4.4}$$

and the do the following transformation

$$\nabla \to i\mathbf{k},\ \frac{\partial}{\partial t} \to -i\omega. \tag{4.5}$$

Also, we want to get rid of the current, so we utilize Ohm's law:

$$\mathbf{J} = \bar{\sigma}\cdot\mathbf{E}, \tag{4.6}$$

where $\bar{\sigma}$ is the conductivity tensor. This turns (4.3) into

$$\left(\left(\mathbf{k^2} - \frac{\boldsymbol{\omega^2}}{\mathbf{c^2}}\right)\bar{\mathbf{I}} - \mathbf{kk} - \mathbf{i}\boldsymbol{\omega\mu_0\bar{\sigma}}\right)\cdot\mathbf{E_1} = 0, \tag{4.7}$$

which is a tensor equation whose solutions are found by setting the determinant equal to zero:

$$\det\left(\left(k^2 - \frac{\omega^2}{c^2}\right)\bar{\mathbf{I}} - \mathbf{kk} - i\omega\mu_0\bar{\sigma}\right) = 0. \tag{4.8}$$

One may now define the *dielectric tensor* as

$$\bar{\varepsilon} = \bar{\mathbf{I}} + \frac{i\bar{\sigma}}{\omega\varepsilon_0} \tag{4.9}$$

and then get

$$\det\left(\frac{k^2c^2}{\omega^2}\left(\frac{\mathbf{kk}}{k^2} - \bar{\mathbf{I}}\right) + \bar{\varepsilon}\right) = 0. \tag{4.10}$$

This is the *general dispersion relation* of a wave in a plasma. To find specific solutions, or modes, one has to find an expression for $\bar{\varepsilon}$.

4.1.1 Cold Plasma Approximation

Let's make some simplifications. To start with, assume that the plasma consists of *cold* electrons, and that the ions are merely a stationary background that ensures quasi-neutrality. The thermal speed of the electrons is smaller than the phase speeds of the waves we are seeking, so the frequency of the solutions will be above the ion cyclotron or plasma frequencies[4].

The dielectric tensor for a cold plasma can be found from the momentum equation, rewritten using the linearized quantities and plane wave approximation;

$$-i\omega \mathbf{v}_1 = \frac{q}{m}(\mathbf{E}_1 + \mathbf{v_1}\times\mathbf{B_0}.) \tag{4.11}$$

Solving this for each component of $\mathbf{v}_1$, gives

$$\begin{aligned} v_x &= \frac{q}{m}\frac{i\omega E_x - \omega_{ce}E_y}{\omega^2-\omega_{ce}^2}, && (4.12)\\ v_y &= \frac{q}{m}\frac{i\omega E_y + \omega_{ce}E_x}{\omega^2-\omega_{ce}^2}, && (4.13)\\ v_z &= \frac{q}{m}\frac{iE_z}{\omega}. && (4.14) \end{aligned}$$

Since $\bar{\sigma}\cdot\mathbf{E} = \mathbf{J} = n_0 q\mathbf{v}_1$, we can write $\bar{\sigma}$ as

$$\bar{\sigma} = \varepsilon_0\omega_{pe}^2 \begin{pmatrix} \frac{i\omega}{\omega^2-\omega_{ce}^2} & \frac{\omega_{ce}}{\omega^2-\omega_{ce}^2} & 0 \\ -\frac{\omega_{ce}}{\omega^2-\omega_{ce}^2} & \frac{i\omega}{\omega^2-\omega_{ce}^2} & 0 \\ 0 & 0 & \frac{i}{\omega} \end{pmatrix}. \tag{4.15}$$

This expression is then used to find $\bar{\varepsilon}$, which is then put into the general dispersion relation (4.3), to get the *cold plasma dispersion relation*. Writing in terms of the index of refraction $\mathbf{n} = \mathbf{k}c/\omega$, and, letting $k_y = 0$, $k_\perp = k_x$, $k_\parallel = k_z$ gives

$$\det\begin{pmatrix} n_\parallel^2 - \varepsilon_{xx} & -\varepsilon_{xy} & -n_\parallel n_\perp \\ \varepsilon_{xy} & n^2-\varepsilon_{xx} & 0 \\ -n_\parallel n_\perp & 0 & n_\perp^2 - \varepsilon_{zz} \end{pmatrix} = 0, \tag{4.16}$$

which is the cold plasma dispersion relation. From this, different wave solutions can be found. we shall derive two solutions, both for parallel propagation. Hence, $\mathbf{k}\cdot\mathbf{B_0} = 0$ and $n_\parallel = n$. This reduces (4.16) to

$$-\varepsilon_{zz}\left(\left(n^2-\varepsilon_{xx}\right)^2 - \varepsilon_{xy}^2\right) = 0. \tag{4.17}$$

The trivial solution $\varepsilon_{zz} = 0$ gives

$$\omega^2 = \omega_{pe}^2. \tag{4.18}$$

This is the dispersion relation for plasma oscillations, and

$$\omega_{pe}^2 = \frac{n_0 q^2}{m\varepsilon_0} \tag{4.19}$$

is the *electron plasma frequency*, the natural oscillation frequency of an electron plasma. In most magnetospheric plasmas, $\omega_{pe} > \omega_{ce}$. the ionosphere being the exception. The equation (4.18) could have been derived directly from the continuity, momentum, and Poisson equations as well.

Whistler Waves

The next set of solutions to (4.17) are

$$n_R^2 = 1 - \frac{\omega_{pe}^2}{\omega(\omega - \omega_{ce})} \tag{4.20}$$

$$n_L^2 = 1 - \frac{\omega_{pe}^2}{\omega(\omega + \omega_{ce})}. \tag{4.21}$$

The subscripts R and L refer to right-handed and left-handed, respectively, i.e. left or right polarized. The right-handed solution can, at frequencies below ω_{ce} (but still above ω_{ci} and ω_{pi}), be rewritten as

$$\omega = \frac{\omega_{ce}}{1 + \frac{\omega_{pe}^2}{k^2c^2}}. \tag{4.22}$$

This wave mode has the interesting property that its phase velocity, $v_{ph} = \omega/\mathbf{k}$, and group velocity, $v_g = \frac{\partial\omega}{\partial\mathbf{k}}$ are both dependent on the frequency:

$$v_{ph} = \frac{c}{n} = \frac{c}{\omega_{pe}\sqrt{\omega\omega_{ce}}}, \tag{4.23}$$

and

$$v_g = \frac{\partial\omega}{\partial k} = 2c\sqrt{\frac{\omega\omega_{ce}}{\omega_{pe}^2}}. \tag{4.24}$$

The effect is that higher frequencies will travel faster from their source and thus be the first to be detected. If one converts these waves into sound waves of the same frequency, they sound as a sort of whistle, from high to low frequencies, so they are simply called *whistler waves*. One way to generate whistler waves occur is in thunderstorms. The electromagnetic disturbance can then be guided along the magnetic field of the Earth to the opposite hemisphere[3].

4.1.2 Hot Plasma Dispersion Relation

Most space plasmas cannot be accurately described using the cold plasma dispersion relation. Instead, one must include thermal effects and then derive the *hot plasma dispersion relation*. we simply present this dispersion relation here,but the astute reader is referred to Swanson[45] for the full derivation. The full dispersion relation reads

$$\begin{aligned} &\left(\gamma\left(\gamma - \kappa_0 + k_\perp^2\right) + \kappa_2^2\right)\kappa_3 + k_\perp^2\left(\left(\gamma - \kappa_0 + k_\perp^2\right)\kappa_1 - \kappa_2^2\right) \\ + \; &\kappa_4\left(\gamma - \kappa_0 + k_\perp^2\right)\left(2k_\perp k_z + \kappa_4\right) - \kappa_5\left(\gamma\kappa_5 + 2\kappa_2\left(k_\perp k_z + \kappa_4\right)\right) = 0, \end{aligned} \tag{4.25}$$

where $\gamma = k_z^2 - \kappa_1$, $\kappa_i = \omega^2/c^2 K_i$, and K_i are elements of the hot dielectric tensor.

Langmuir Waves

The plasma oscillations mentioned previously become modified when the plasma is hot. To see this, one must add the pressure term $-\nabla \mathsf{P}$ to the momentum equation. The dispersion relation does get a little bit easier, however, if we consider parallel propagating waves at high frequencies. In this case, the dielectric tensor is identical to that of the cold plasma, if one simply makes the replacement

$$\varepsilon_{zz} = 1 - \frac{\omega_{pe}^2}{\omega^2} \rightarrow 1 - \frac{\omega_{pe}^2}{\omega^2 - \gamma_e v_{th}^2}, \tag{4.26}$$

where γ_e is the adiabatic index. Setting $\varepsilon_{zz} = 0$ gives

$$\omega^2 = \omega_{pe}^2 + \gamma_e k^2 v_{th}^2, \tag{4.27}$$

which is the dispersion relation for *Langmuir waves*.

4.1.3 Dispersion Surfaces

The dispersion relations can be visualized by plotting ω as a function of the wavenumber k, for some angle, usually the perpendicular or parallel directions. In doing so, one can see the relations between the different wave modes in a plasma and their properties. For example, the slope of the curve at any point gives the group velocity, while the slope of the line extending from the origin to the point of interest gives the phase velocity.

Some other properties that can be read from the dispersion relation are *cut-offs* and *resonances*. A cut-off occurs at the points where k^2 becomes less than zero. This has no real valued solutions for $\mathbf{k}$, so the wave cannot propagate, as its phase velocity will not be defined. A wave propagating into a region where its wave vector would become complex will be reflected at that point. For example, radio waves sent from a ground station up into the ionosphere will reflect when it encounters a region where the electron plasma frequency is greater than the frequency of the wave. This is exploited in long-wave radio communication, as it allows two radio stations to transmit and receive signals that would otherwise be blocked by the curvature of the Earth. A resonance, on the other hand, is when the wave number approaches infinity. In other words, the wavelength becomes very small. One good way of visualizing the different wave modes is to plot *dispersion surfaces* (André, 1985), These are like dispersion plots, but with the whole angular dependence of the modes viewable as well. One displays the wave frequency (usually normalized to the cyclotron or plasma frequency of the interesting particle species), against the parallel and perpendicular wave numbers in a three-dimensional plot. Figure 4.1 shows one example of such a plot, in this case it shows a few different wave modes in a hot plasma. No ion waves are shown in the figure. The dispersion relations are solved using the WHAMP, Waves in Hot, Anisotropic, Magnetized Plasmas[42].

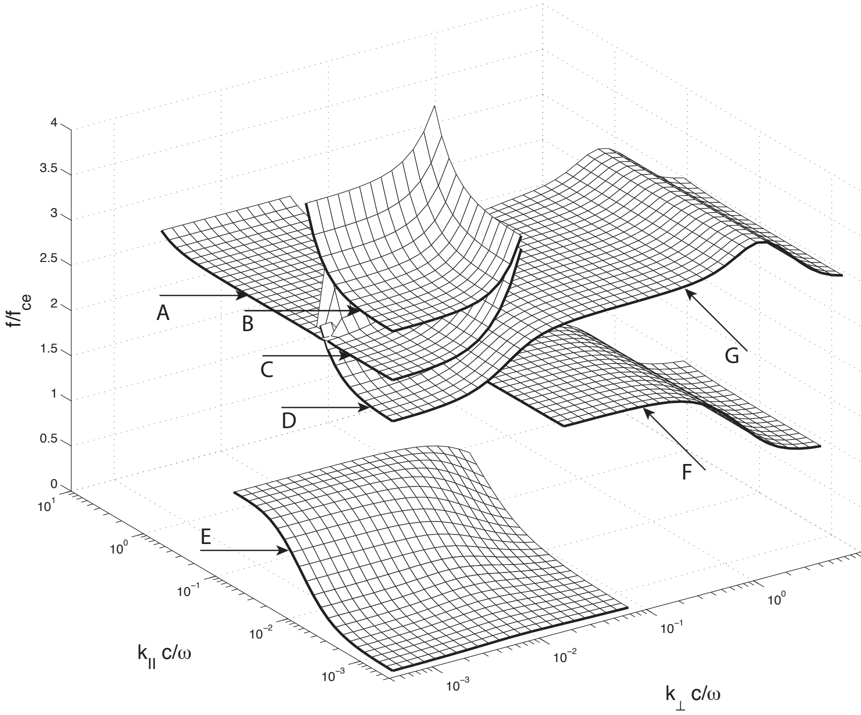

Figure 4.1. Dispersion surfaces for some of the wave modes in a warm plasma with $f_{pe} > f_{ce}$. The horizontal axes show the parallel and perpendicular wave numbers, normalized with c/ω_{ce}, and the vertical axis shows the frequency, normalized to ω_{ce}. The surfaces are generated using WHAMP[42].

Plasma waves can be categorized in several ways. One separates *electrostatic* waves from *electromagnetic* ones, as the former has no magnetic field fluctuations. Waves can also be labelled according to the direction of their wave vector with respect to the magnetic field. *Parallel* waves propagate along **B**, whereas *perpendicular* ones propagate at 90 degrees. Waves may also travel at any intermediate angle. *Longitudinal* waves have the wave electric field in the same direction as the wave vector, while *transverse* waves have $\mathbf{E} \perp \mathbf{k}$. The polarization of the wave can be *left-handed*, i.e. the wave electric field rotates in the opposite sense as electrons do around a magnetic field line, as opposed to *right-handed* waves.

Let's take a closer look at Figure 4.1 to see which types of waves are represented. The surfaces were generated by assuming a plasma with $f_{pe} = 1.5 f_{ce}$, a so called *over-dense* plasma. Also, we let the ion-to-electron mass ratio be 1836, i.e. the ions are all protons. The two horizontal axes show the normalized parallel and perpendicular wave numbers, respectively, in logarithmic scale. The vertical axis shows the frequency, normalized to the electron cyclotron frequency, in linear scale.

Parallel Propagation
Surface A in Figure 4.1 represents a short wavelength Langmuir wave. The group velocity starts to increase as $k_\parallel$ increases, in accordance with (4.27). B denotes the so-called *R-mode*, which is an electromagnetic, right-hand polarized wave. Looking at the surface labelled C, we see the long wavelength Langmuir wave. Surface D marks a left-hand polarized wave, usually called just the *L-mode*. Surface A and D are actually the same surface, changing characteristics at $k_\parallel c/\omega \approx 10^{-2}$. The phase velocity of both the R-mode and the L-mode approaches the speed of light as $k_\parallel$ increases. Surface E is the whistler wave branch. The surface approaches, but never reaches, $f = f_{ce}$, so whistler waves must only exist below the electron cyclotron frequency. They also have a cut-off above the ion cyclotron frequency[1].

Perpendicular Propagation
For propagation perpendicular to the magnetic field, surface C represents an electromagnetic wave whose dispersion relation is

$$\omega^2 = \omega_{pe}^2 + k_\perp^2 c^2, \tag{4.28}$$

which becomes an ordinary electromagnetic wave for vanishing ω_{pe}. Hence, this mode is simply called the *ordinary mode*, or *O-mode*. This mode has a cut-off at the plasma frequency. The perpendicular part of surface D, together with the perpendicular part of surface B, is called the *extra-ordinary mode*, or *X-mode* and is an electromagnetic wave as well. F shows one of the *electrostatic Bernstein modes*. These are separated by a frequency gap of f_{ce}, but only one Bernstein mode is shown here. G is the *upper-hybrid plateau*. The hump seen at large $k_\perp$ is a thermal effect. The phase velocity of the upper branch of the X-mode approaches that of the O-mode, i.e. the speed of light[1].

4.2 Observations

Plasma theory is important, but to actually know what is happening in space, we need satellite measurements. Plasma waves are detected by electric and magnetic field instruments, e.g. STAFF, EFW, and WBD on Cluster. Let's take waves in the electric field as an example. The EFW instrument on Cluster measures the potential between the different probes and between the probes and the spacecraft. Once we know the potential difference between two probes, we divide this with the distance between the probes to get the electric field. The electric field is measured in the spacecraft inertial frame. We therefore have to transform the data into another coordinate system, e.g. *geocentric solar magnetic*, GSM, which has its x-axis pointing along the Sun-Earth line, with positive direction towards the Sun. The z-axis is parallel to the Earth's magnetic axis, and the y-axis is formed by the cross-product of the z- and x-axes. Now we can look at the variations of this electric field, in the shape of its *waveform*, such as seen on panels 1, 3, and 5 in Figure 4.2, taken from[50]. The waveforms look nice, but it is also useful to see which frequencies are dominant in the signal. Fourier analysis states that a signal can be described as a sum of its Fourier components[16], which gives information of how much power is in different frequencies To calculate the spectrum, we use the *fast Fourier transform*, FFT, giving a line spectrum as those in panels 2, 4, and 6 in Figure 4.2. Now we can observe the dominant frequencies as peaks in the spectrum. However, in calculating a spectrum of a time series, we lose all information about time variation, the spectrum is an average for that time period. If we want both temporal and spectral information, we can divide the signal into smaller parts and calculate the spectrum for each part. These individual spectra are then combined to form a *spectrogram*, is a two-dimensional image with frequency on one axis and time on the other. The amplitude of the signal is then represented by color.

In Figure 4.3 is shown a spectrum that has been calculated from the electric field data recorded by the WBD instrument. Three wave types are labelled: *electrostatic solitary waves* (ESWs), *electron cyclotron waves* (EC), and Langmuir waves. ESWs appear in the spectra as broadbanded electrostatic noise. Matsumoto, et al.[31] showed that much of such noise in the magnetosphere was actually ESWs. EC waves appear as sharp signals just above the electron cyclotron frequency and propagate perpendicularly to the magnetic field. Langmuir waves also have a narrow bandwidth, with a frequency just above the electron plasma frequency, as given by (4.27). The spectral content of a signal does not contain all the information that we can get. We can also look at the polarization of the wave if we have measurements along more than one dimension. Using magnetic wave data gives us information on whether a wave is electrostatic or electromagnetic. Also, the *Poynting flux* can then be determined. This is the flux of energy in an electromagnetic wave, and is calculated as

$$\mathbf{P} = \frac{\delta\mathbf{E} \times \delta\mathbf{B}}{\mu_0}, \tag{4.29}$$

where $\delta\mathbf{E}$ and $\delta\mathbf{B}$ is the wave electric and magnetic fields, respectively. The Poynting flux points in the same direction as the group velocity of the wave[4].

4.3 Waves in Reconnection

Reconnection can create particle distributions that are unstable, such as the *bump-on-tail* and *two-stream* distributions, examples of which are seen in Figure 4.4. As these instabilities are relaxed, waves are generated that can be measured by at higher resolution than is available for particle instruments.

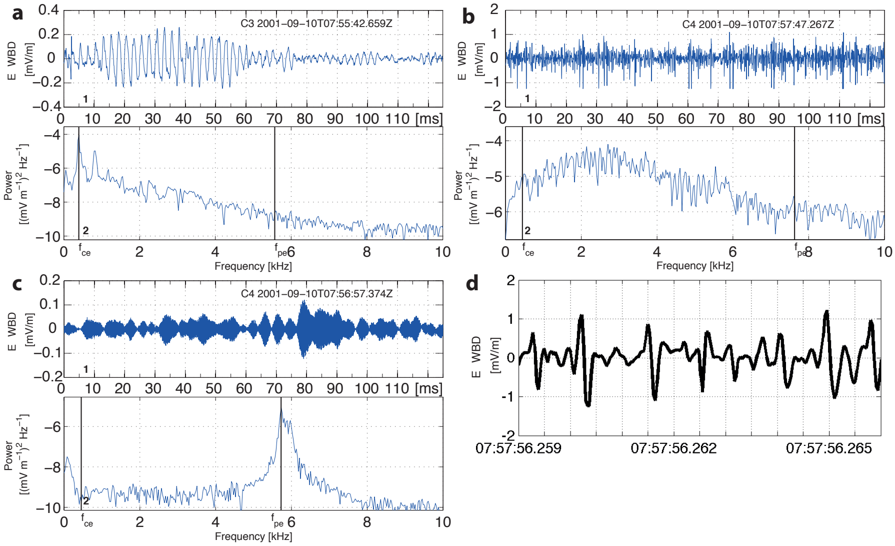

Figure 4.2. Waveforms and spectra of three wave types observed by the Cluster WBD instrument. From panel a-c are electron cyclotron (EC) waves, electrostatic solitary waves (ESWs), and Langmuir waves. The EC and Langmuir waves have clear peaks in their spectra near f_{ce} and f_{pe}, respectively. The ESWs show up as broadband noise in the spectrum. All waveforms have a duration of 125 ms, except the last, which is 6 ms long. The last waveform, in panel d, is a close-up of an ESW waveform, showing the bipolar structure of the waves. The vertical lines mark f_{ce} and f_{pe}, respectively. The figure is adapted from [50].

Plasma waves play an important part in magnetic reconnection: they can interact strongly with the plasma, causing acceleration and heating of different plasma species. It is speculated that waves may also be a cause of the anomalous resistivity needed for the onset of reconnection [21,49]. Strong plasma waves may also be mode converted into radio emissions that can escape the wave generation region and be detected by remote observation. This could allow scientists to examine e.g. solar flares, where magnetic reconnection is thought to be important, but no spacecraft can do measurements *in situ*.

Many plasma wave modes have been confirmed, or inferred by theory and simulations, to exist in relation to magnetic reconnection. Most wave activity appears to take place in the separatrix regions of the reconnection structure. Here, parallel electric fields develop that accelerate electrons along the magnetic field to form energetic beams. These beams give rise to plasma distributions that are unstable to various wave modes.

We now discuss briefly some of the wave modes that are known or expected to exist in relation to magnetic reconnection. Matsumoto, et al. [30] observed ESWs in relation to magnetopause reconnection and Khotyaintsev, et al. [25] observed these waves during magnetotail reconnection, generated by an electron

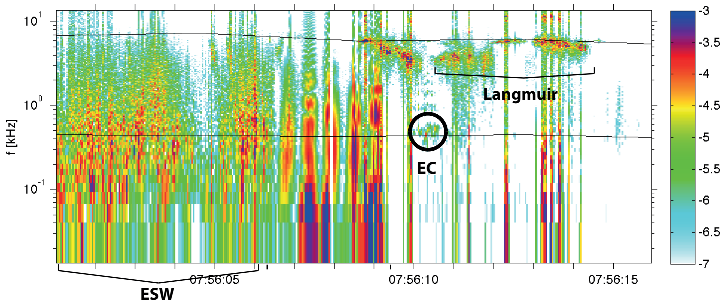

Figure 4.3. Spectrogram of an event where the three wavetypes from Figure 4.2 occurred close to each other. The broadbanded nature of ESWs and the small bandwidth of EC and Langmuir waves are clearly seen. The strong signal between the ESWs and EC waves is an effect of the WHISPER instrument on Cluster, and not a real wave phenomenon. The black lines show f_{ce} and f_{pe}, respectively. The resolution of f_{ce} is not that good at all times., hence it appears to bel above the Langmuir frequency. The Figure is adapted from[50].

beam. In another paper by Khotyaintsev, et al.[24] observed Langmuir and/or upper-hybrid waves in the cusp region of the Earth's magnetosphere and argue that they are caused by electron beams generated at a distant X-line. Deng, et al.[12] also observed Langmuir waves, in this case in the magnetotail.

Another wave type that is frequently observed in the reconnection region is the whistler mode[54]. Whistler waves have been suggested as an important mechanism for accelerating plasma during reconnection[5]. Deng, et al.[11] observed whistler waves during magnetic reconnection at the magnetopause. Whistler waves can be generated by several mechanisms, one of them being an electron beam[54], with such high energies, that reconnection seems the most likely acceleration mechanism. Whistler waves propagate at an angle to

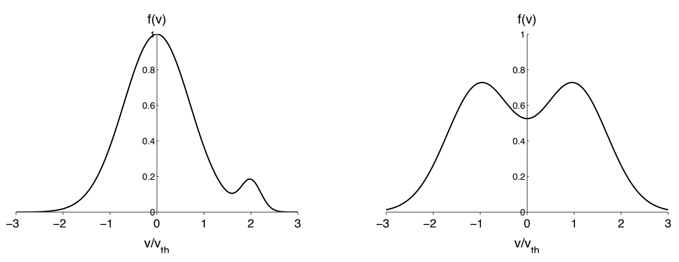

Figure 4.4. Left: Nump-on-tail distribution, with a thermal background and a cold electron beam att speed $v_d = 2v_{th}$. Right: Two-stream distribution consisting of two, equally dense beams travelling at the same speed.

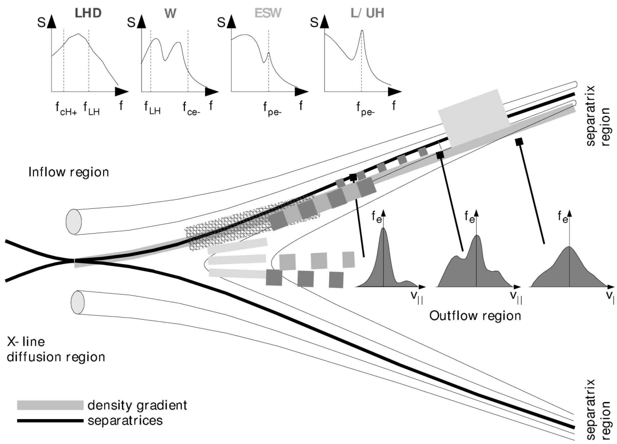

Figure 4.5. Schematic view of the reconnection separatrix region. Locations of different wave generation is marked, and the distribution functions for different locations are illustrated. Figure is from Vaivads, et al. (2006)[48].

the magnetic field, and may travel large distances, making the ideal for remote studies of reconnection.

A last wave type to be discussed is the electron cyclotron, EC, wave. As mentioned previously, this mode is an electrostatic wave with phase velocity perpendicular to the magnetic field. EC waves have been speculated to exist in the reconnection region, but searches for them has been fruitless. Also here may electron beams be responsible for the wave generation. Menietti, et al.[33] observed EC waves in the polar cap. They also made numerical calculations showing that a low-energy electron beam could drive EC waves, if there also existed a very cold electron background population.

The detailed spatial structure of the separatrix region is not well understood, but Vaivads, et al.[48] draws a simplified picture with some of the above mentioned wave types included. The whistler waves are typically observed close to the X-line, in the current sheet. ESWs and Langmuir/upper-hybrid waves, on the other hand, are observed in the separatrix regions. The fine-scaled structure, i.e. where inside the separatrix regions these waves occur, is not shown. In the top of Figure 4.5, spectra of different modes are shown. The ESW and Langmuir/UH spectra resemble those displayed in Figure 4.2. The whistler mode is seen to have a peak somewhere between the lower-hybrid (LH) and electron cyclotron frequencies.

5. Into the Unknown

> *Derek says it's always good to end a paper with a quote. He says someone else has already said it best. So if you can't top it, steal from them and go out strong.*
>
> – Edward Furlong, *American History X*

In this thesis we study, in Paper I, high-frequency electrostatic and electromagnetic waves in relation to magnetic reconnection in the Earth's magnetotail and, in Paper II, whistler waves in relation to dipolarization fronts.

In Paper I, we show that the main source region for the high-frequency waves is the separatrix region. We also show that the separatrix region is stratified, having sharp boundaries between regions of different characteristics. In Paper II, we find that magnetotail dipolarization fronts are often associated with whistler waves. In this chapter, we discuss the relevance of our research and the implications of our results.

5.1 Magnetic Reconnection and High-Frequency Waves

Magnetic reconnection is a universal plasma phenomenon, capable of converting large amounts of magnetic energy into kinetic energy and heat of plasma particles. Solar flares are suspected to be caused by magnetic reconnection. The extreme conditions close to the Sun make *in situ* observations impossible, so we are restricted to remote sensing of the solar flares. This approach has some obvious drawbacks. First, it limits the spatial resolution drastically, making it difficult to observe the fine structure of the reconnection region. Second, information of the particles is not available. Third, we are limited to line-of-sight observations and cannot get a three-dimensional picture of the reconnection region.

Magnetic reconnection in the Earth's magnetosphere can and has been studied, and in increasingly high detail. Since the only way to study reconnection at the Sun is by electromagnetic emissions, we would like to find a connection between such emissions and the reconnection processes in the magnetosphere. In the solar corona, electromagnetic emissions of various types are observed, and among these are Type-III solar radio bursts. These are caused by highly energetic electron beams travelling along the magnetic field lines out from the Sun. The electromagnetic emissions are generated by mode conversion of Langmuir waves at the local plasma frequency, and its first harmonic[32]. Since

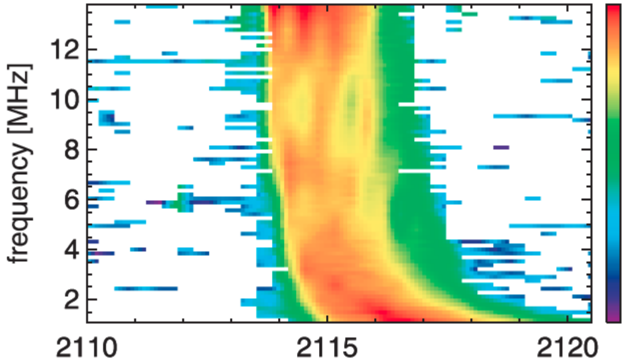

Figure 5.1. Type-III solar radio burst recorded by the WIND/WAVES instrument onboard RHESSI[27]. The time is given as hours and minutes.

the plasma frequency is proportional to the square root of the plasma density, the frequency of the Type-III emissions will decrease as the electron beam travels away from the Sun. This gives the Type-III emissions their characteristic appearance in a spectrogram, as seen in Figure 5.1.

A first step towards a picture of the electromagnetic emissions at reconnection sites is to map different high-frequency waves to the magnetic reconnection structure. This is the topic of our first study. For details we refer the reader to Paper I.

5.2 Whistler Waves and Dipolarization Fronts

Magnetic reconnection can be a steady or a transient phenomenon. It is known that transient, or unsteady, reconnection can accelerate particles to very high energies[20]. It has also been shown that dipolarization fronts are signatures of transient reconnection[44].

In Paper II, we study the correlation between dipolarization fronts and whistler waves. Whistler waves have been previously observed in relation to dipolarization fronts, but no comprehensive statistical study has been done. It is found that whistlers are very common at dipolarization fronts, making them a useful tool to infer the existence of DFs. This is especially useful for e.g. planetary missions, where particle data may not be available, or of insufficient quality. Also, since whistlers can be a signature of DFs, they can also be a signature of transient magnetic reconnection.

5.3 Outlook

For our next study, we will focus our attention to the dayside magnetosphere and make a survey of whistler waves near the magnetopause. Whistler waves can be a signature of open magnetic field lines, ans thus of ongoing magnetic reconnection. The approach will be similar to that of our study of whistler waves at dipolarization fronts.

6. Summary of papers

Paper I: Mapping HF Waves in the Reconnection Diffusion Region

Authors: H. Viberg, Y. V. Khotyaintsev, A. Vaivads, M. André, and J. S. Pickett
Journal: Geophysical Research Letters
Status: Published

Waves are very important in the reconnection process. The onset of reconnection may be a result of an anomalous resistivity, caused by waves scattering particles. Also, waves relax steep plasma gradients and currents. This means that to observe waves is to observe the particle dynamics on scales so small that they may not be accessible to particle instruments.

High frequency waves are often observed at reconnection sites. Electrostatic solitary waves (ESWs) where observed in the magnetotail[8,25], and at the magnetopause[40]. Langmuir waves have been observed by several authors as well[18,47,24]. The existence of electron cyclotron waves have been proposed[48], but this wave type has eluded detection.

In this paper we make a detailed case study of a reconnection event, previously identified by Eastwood, et al.[15] We employ the WBD[22] instrument to resolve high-frequency waveforms, and PEACE[35] data to analyze the electron distribution at sub-spin (125 ms) resolution. Using sub-spin resolution data together with the continuous WBD waveform allows us to make direct comparison between electron distributions and observed waves. The advantage of using WBD data is its high time-resolution, allowing us to really observe the detailed structures of the wave electric field as the satellites pass the reconnection region.

Three main types of waves are observed: electron cyclotron (EC), Langmuir, and electrostatic solitary waves (ESWs). This is the first time that EC waves have been observed at a reconnection site. We map all three wave types to the separatrix regions. In more detail, the ESWs are observed close to the ion outflow region, whereas the EC and Langmuir waves are located closer to the inflow region. The EC waves are generally observed further away from the flow reversal. The separatrix region is found to be stratified, with one wave type being observed for several seconds and then, within milliseconds, the nature of the waves have completely changed. At a velocity of 200-400 km/s (roughly the bulk ion velocity in the separatrix regions), 50 ms corresponds roughly to about 1-2 times the electron inertial length. The ESWs are typically associated with counter-streaming electron beams, giving rise to a two-stream instability, which is known to generate ESWs[34]. Langmuir waves can be generated by the bump-on-tail instability caused by a beam of electrons moving along the magnetic field[34], and such distributions are indeed observed in conjunction with the Langmuir waves. Together with the EC waves we see rather isotropic flat-top distributions. However, we cannot conclude that this distribution is unstable to EC waves, since we are unable to resolve the low-energy part of the distribution, and cannot rule out low-energy electron beams, which have been suggested to be a cause of EC waves[33].

Detailed mapping of HF waves at reconnection sites is important for resolving small-scale structures in the reconnection region, and to better understand the electron dynamics.

Paper II: Whistler Mode Waves at Magnetotail Dipolarization Fronts

Authors: H. Viberg, Y. V. Khotyaintsev, A. Vaivads, M. André, H. S. Fu, and N. Cornilleau-Wehrlin

Journal: Geophysical Research Letters
Status: In preparation

A *dipolarization front*, DF, is identified as a sharp gradient in the z-component of the magnetic field and associated with fast plasma flows and energetic particles. DFs are a sign of transient, or unsteady, magnetic reconnection taking place tailward of the DF. Transient magnetic reconnection is able to accelerate particles to very high energies[20].

Whistler waves are right-hand polarized waves with frequencies between the lower-hybrid, f_{LH}, and the electron cyclotron frequencies, f_{ce}. They are commonly observed in the magnetotail, and can propagate a long distance from their generation region, along the geomagnetic field. Several case studies show that DFs are associated with whistler waves, generated by the perpendicular electron temperature anisotropy that results from the increased magnetic field of the DF. A statistical knowledge of the occurrence of whistlers at DFs can be a useful tool for identifying DFs, especially when particle data is not of sufficient quality, for example on planetary missions.

In this paper we present a statistical survey of whistler waves at DFs in the Earth's magnetotail over nine years of Cluster data. More specifically, we make use of data from the STAFF[9], CIS[39], FGM[2], PEACE[35], and EFW[23] instruments. The z-component of the magnetic field, supplied by FGM, is searched for dipolarization fronts by fitting a hyperbolic tangent function to the data. Using the same criteria as in[19], more than 1200 DF events are found. For these times we then use data about the power spectral density, the degree of polarization, and the ellipticity of the wave magnetic field. These datasets are searched for signatures characteristic of whistler waves; right-hand polarization and frequency range between f_{LH} and f_{ce}. We also require the signals to have sufficiently long duration in time and to be continuous in frequency. The events that pass this process are considered to be whistler waves and subject to statistical analysis.

We found that whistler waves are very common at DFs, with about 30-60% of the DFs being associated with them. We compared to the probability of finding whistlers at any point in the Earth's magnetotail, and found that the likelihood is 20-40 times higher of finding the waves at a DF. Thus we conclude that whistler waves are important in the dynamics of the magnetosphere and that they are indeed useful as a tool for identifying DFs.

References

1. M. André. Dispersion surfaces. *Journal of Plasma Physics*, 33:1–19, February 1985.
2. A. Balogh, P. J. Cargill, C. M. Carr, M. W. Dunlop, T. S. Horbury, E. A. Lucek, and Cluster FGM Investigator Team. Magnetic Field Observations on Cluster: an Overview of the First Results. In B. Warmbein, editor, *Sheffield Space Plasma Meeting: Multipoint Measurements versus Theory*, volume 492 of *ESA Special Publication*, page 11, January 2001.
3. Heinrich Barkhausen. Whistling tones from the earth. *Proceedings of the Institute of Radio Engineers*, 18(7):1155–1159, 1930.
4. W. Baumjohann and R.A. Treumann. *Basic Space Plasma Physics*. Imperial College Press, 1997.
5. J. Birn, J. F. Drake, M. A. Shay, B. N. Rogers, R. E. Denton, M. Hesse, M. Kuznetsova, Z. W. Ma, A. Bhattacharjee, A. Otto, and P. L. Pritchett. Geospace Environmental Modeling (GEM) magnetic reconnection challenge. *J. Geophys. Res.*, 106:3715–3720, March 2001.
6. D. Biskamp. *Magnetic Reconnection in Plasmas*. September 2000.
7. T. J. M. Boyd and J. J. Sanderson. *The Physics of Plasmas*. January 2003.
8. C. Cattell, J. Dombeck, J. Wygant, J. F. Drake, M. Swisdak, M. L. Goldstein, W. Keith, A. Fazakerley, M. André, E. Lucek, and A. Balogh. Cluster observations of electron holes in association with magnetotail reconnection and comparison to simulations. *Journal of Geophysical Research (Space Physics)*, 110:1211, January 2005.
9. N. Cornilleau-Wehrlin, G. Chanteur, S. Perraut, L. Rezeau, P. Robert, A. Roux, F. Sahraoui, G. Belmont, T. Chust, O. Le Contel, M. Maksimovic, D. Hubert, C. Lacombe, F. Lefeuvre, M. Parrot, J. Pincon, P. M. Décréau, C. C. Harvey, P. Louarn, W. Kofman, O. Santolik, D. A. Gurnett, H. S. Alleyne, M. P. Gough, M. Andre, G. Gustafsson, A. Pedersen, M. Roth, R. Pellinen, and A. Balogh. First Results of the Spatio-Temporal Analysis of Field Fluctuations Experiment (STAFF) of Cluster. *AGU Fall Meeting Abstracts*, page C3, December 2001.
10. P. M. E. Décréau, P. Fergeau, V. Krannosels'kikh, M. Leveque, P. Martin, O. Randriamboarison, F. X. Sene, J. G. Trotignon, P. Canu, and P. B. Mogensen. Whisper, a Resonance Sounder and Wave Analyser: Performances and Perspectives for the Cluster Mission. *Space Sci. Rev.*, 79:157–193, January 1997.
11. X. H. Deng and H. Matsumoto. Rapid magnetic reconnection in the Earth's magnetosphere mediated by whistler waves. *Nature*, 410:557–560, March 2001.

12. X. H. Deng, H. Matsumoto, H. Kojima, T. Mukai, R. R. Anderson, W. Baumjohann, and R. Nakamura. Geotail encounter with reconnection diffusion region in the Earth's magnetotail: Evidence of multiple X lines collisionless reconnection? *Journal of Geophysical Research (Space Physics)*, 109:5206, May 2004.

13. J. W. Dungey. The motion of magnetic fields. *Mon. Not. R. Astron. Soc.*, 113:679, 1953.

14. J. P. Eastwood. The science of space weather. *Royal Society of London Philosophical Transactions Series A*, 366:4489–4500, December 2008.

15. J. P. Eastwood, T. D. Phan, M. Øieroset, and M. A. Shay. Average properties of the magnetic reconnection ion diffusion region in the Earth's magnetotail: The 2001-2005 Cluster observations and comparison with simulations. *Journal of Geophysical Research (Space Physics)*, 115:8215, August 2010.

16. A. I. Eriksson. Spectral Analysis. *ISSI Scientific Reports Series*, 1:5–42, 1998.

17. C. P. Escoubet, R. Schmidt, and M. L. Goldstein. Cluster - Science and Mission Overview. *Space Sci. Rev.*, 79:11–32, January 1997.

18. W. M. Farrell, M. D. Desch, M. L. Kaiser, and K. Goetz. The dominance of electron plasma waves near a reconnection X-line region. *Geophys. Res. Lett.*, 29:1902, October 2002.

19. H. S. Fu, Y. V. Khotyaintsev, A. Vaivads, M. André, and S. Y. Huang. Occurrence rate of earthward-propagating dipolarization fronts. *Geophys. Res. Lett.*, 39:10101, May 2012.

20. H. S. Fu, Y. V. Khotyaintsev, A. Vaivads, A. Retinò, and M. André. Energetic electron acceleration by unsteady magnetic reconnection. *Nature Physics*, 9:426–430, July 2013.

21. M. Fujimoto, I. Shinohara, and H. Kojima. Reconnection and Waves: A Review with a Perspective. *Space Sci. Rev.*, 160:123–143, October 2011.

22. D. A. Gurnett, R. L. Huff, and D. L. Kirchner. The Wide-Band Plasma Wave Investigation. *Space Sci. Rev.*, 79:195–208, January 1997.

23. G. Gustafsson, M. André, T. Carozzi, A. I. Eriksson, C.-G. Fälthammar, R. Grard, G. Holmgren, J. A. Holtet, N. Ivchenko, T. Karlsson, Y. Khotyaintsev, S. Klimov, H. Laakso, P.-A. Lindqvist, B. Lybekk, G. Marklund, F. Mozer, K. Mursula, A. Pedersen, B. Popielawska, S. Savin, K. Stasiewicz, P. Tanskanen, A. Vaivads, and J.-E. Wahlund. First results of electric field and density observations by Cluster EFW based on initial months of operation. *Annales Geophysicae*, 19:1219–1240, October 2001.

24. Y. Khotyaintsev, A. Vaivads, Y. Ogawa, B. Popielawska, M. André, S. Buchert, P. Décréau, B. Lavraud, and H. Rème. Cluster observations of high-frequency waves in the exterior cusp. *Annales Geophysicae*, 22:2403–2411, July 2004.

25. Y. V. Khotyaintsev, A. Vaivads, M. André, M. Fujimoto, A. Retinò, and C. J. Owen. Observations of Slow Electron Holes at a Magnetic Reconnection Site.

Physical Review Letters, 105(16):165002, October 2010.

26. M. G. Kivelson and C. T. Russell. *Introduction to Space Physics*. April 1995.
27. S. Krucker, E. P. Kontar, S. Christe, and R. P. Lin. Solar Flare Electron Spectra at the Sun and near the Earth. *Astrophys. J.*, 663:L109–L112, July 2007.
28. P. Lindqvist, C. Cully, Y.V. Khotyaintsev, and the EFW team. *User Guide to the EFW Measurements in the Cluster Active Archive (CAA)*, 2013.
29. S. Markidis, G. Lapenta, L. Bettarini, M. Goldman, D. Newman, and L. Andersson. Kinetic simulations of magnetic reconnection in presence of a background O^+ population. *Journal of Geophysical Research (Space Physics)*, 116:0, September 2011.
30. H. Matsumoto, X. H. Deng, H. Kojima, and R. R. Anderson. Observation of Electrostatic Solitary Waves associated with reconnection on the dayside magnetopause boundary. *Geophys. Res. Lett.*, 30:1326, March 2003.
31. H. Matsumoto, H. Kojima, T. Miyatake, Y. Omura, M. Okada, I. Nagano, and M. Tsutsui. Electrotastic Solitary Waves (ESW) in the magnetotail: BEN wave forms observed by GEOTAIL. *Geophys. Res. Lett.*, 21:2915–2918, December 1994.
32. D. J. McLean and N. R. Labrum. *Solar radiophysics: Studies of emission from the sun at metre wavelengths*. 1985.
33. J. D. Menietti, O. Santolik, J. D. Scudder, J. S. Pickett, and D. A. Gurnett. Electrostatic electron cyclotron waves generated by low-energy electron beams. *Journal of Geophysical Research (Space Physics)*, 107:1285, October 2002.
34. Y. Omura, H. Matsumoto, T. Miyake, and H. Kojima. Electron beam instabilities as generation mechanism of electrostatic solitary waves in the magnetotail. *Journal of Geophysical Research*, 101:2685–2698, February 1996.
35. C. J. Owen, A. N. Fazakerley, P. J. Carter, A. J. Coates, I. C. Krauklis, S. Szita, M. G. G. T. Taylor, P. Travnicek, G. Watson, R. J. Wilson, A. Balogh, and M. W. Dunlop. Cluster PEACE observations of electrons during magnetospheric flux transfer events. *Annales Geophysicae*, 19:1509–1522, October 2001.
36. E. N. Parker. Sweet's Mechanism for Merging Magnetic Fields in Conducting Fluids. *J. Geophys. Res.*, 62:509–520, December 1957.
37. G. Paschmann, F. Melzner, R. Frenzel, H. Vaith, P. Parigger, U. Pagel, O. H. Bauer, G. Haerendel, W. Baumjohann, N. Scopke, R. B. Torbert, B. Briggs, J. Chan, K. Lynch, K. Morey, J. M. Quinn, D. Simpson, C. Young, C. E. McIlwain, W. Fillius, S. S. Kerr, R. Mahieu, and E. C. Whipple. The Electron Drift Instrument for Cluster. *Space Sci. Rev.*, 79:233–269, January 1997.
38. E. Priest and T. Forbes, editors. *Magnetic reconnection : MHD theory and applications*, 2000.
39. H. Rème, C. Aoustin, J. M. Bosqued, I. Dandouras, B. Lavraud, J. A. Sauvaud, A. Barthe, J. Bouyssou, T. Camus, O. Coeur-Joly, A. Cros, J. Cuvilo, F. Ducay,

Y. Garbarowitz, J. L. Medale, E. Penou, H. Perrier, D. Romefort, J. Rouzaud, C. Vallat, D. Alcaydé, C. Jacquey, C. Mazelle, C. D'Uston, E. Möbius, L. M. Kistler, K. Crocker, M. Granoff, C. Mouikis, M. Popecki, M. Vosbury, B. Klecker, D. Hovestadt, H. Kucharek, E. Kuenneth, G. Paschmann, M. Scholer, N. Sckopke, E. Seidenschwang, C. W. Carlson, D. W. Curtis, C. Ingraham, R. P. Lin, J. P. McFadden, G. K. Parks, T. Phan, V. Formisano, E. Amata, M. B. Bavassano-Cattaneo, P. Baldetti, R. Bruno, G. Chionchio, A. di Lellis, M. F. Marcucci, G. Pallocchia, A. Korth, P. W. Daly, B. Graeve, H. Rosenbauer, V. Vasyliunas, M. McCarthy, M. Wilber, L. Eliasson, R. Lundin, S. Olsen, E. G. Shelley, S. Fuselier, A. G. Ghielmetti, W. Lennartsson, C. P. Escoubet, H. Balsiger, R. Friedel, J.-B. Cao, R. A. Kovrazhkin, I. Papamastorakis, R. Pellat, J. Scudder, and B. Sonnerup. First multispacecraft ion measurements in and near the Earth's magnetosphere with the identical Cluster ion spectrometry (CIS) experiment. *Annales Geophysicae*, 19:1303–1354, October 2001.

40. A. Retinò, A. Vaivads, M. André, F. Sahraoui, Y. Khotyaintsev, J. S. Pickett, M. B. Bavassano Cattaneo, M. F. Marcucci, M. Morooka, C. J. Owen, S. C. Buchert, and N. Cornilleau-Wehrlin. Structure of the separatrix region close to a magnetic reconnection X-line: Cluster observations. *Geophys. Res. Lett.*, 33:6101, March 2006.
41. W. Riedler, K. Torkar, F. Rudenauer, M. Fehringer, A. Pedersen, R. Schmidt, R. J. L. Grard, H. Arends, B. T. Narheim, J. Troim, R. Torbert, R. C. Olsen, E. Whipple, R. Goldstein, N. Valavanoglou, and H. Zhao. Active Spacecraft Potential Control. *Space Sci. Rev.*, 79:271–302, January 1997.
42. K. Roennmark. Waves in homogeneous, anisotropic multicomponent plasmas (WHAMP). Technical report, June 1982.
43. Ingrid Sandahl. *Norrsken : budbärare från rymden*. Atlantis, Stockholm, [ny utg.] edition, 1998.
44. M. I. Sitnov, M. Swisdak, and A. V. Divin. Dipolarization fronts as a signature of transient reconnection in the magnetotail. *Journal of Geophysical Research (Space Physics)*, 114:4202, April 2009.
45. D. G. Swanson. *Plasma waves*. 1989.
46. P. A. Sweet. The Neutral Point Theory of Solar Flares. In B. Lehnert, editor, *Electromagnetic Phenomena in Cosmical Physics*, volume 6 of *IAU Symposium*, page 123, 1958.
47. A. Vaivads, Y. Khotyaintsev, M. André, A. Retinò, S. C. Buchert, B. N. Rogers, P. Décréau, G. Paschmann, and T. D. Phan. Structure of the Magnetic Reconnection Diffusion Region from Four-Spacecraft Observations. *Physical Review Letters*, 93(10):105001, August 2004.
48. A. Vaivads, Y. Khotyaintsev, M. André, and R. A. Treumann. Plasma Waves Near Reconnection Sites. In J. W. Labelle and R. A. Treumann, editors, *Geospace Electromagnetic Waves and Radiation*, volume 687 of *Lecture Notes in Physics, Berlin Springer Verlag*, page 251, January 2006.

49. A. Vaivads, A. Retinò, and M. André. Magnetic reconnection in space plasma. *Plasma Physics and Controlled Fusion*, 51(12):124016, December 2009.

50. H. Viberg, Y. V. Khotyaintsev, A. Vaivads, M. André, and J. S. Pickett. Mapping HF waves in the reconnection diffusion region. *Geophys. Res. Lett.*, 40:1032–1037, March 2013.

51. B. Wilken, W. I. Axford, I. Daglis, P. Daly, W. Guttler, W. H. Ip, A. Korth, G. Kremser, S. Livi, V. M. Vasyliunas, J. Woch, D. Baker, R. D. Belian, J. B. Blake, J. F. Fennell, L. R. Lyons, H. Borg, T. A. Fritz, F. Gliem, R. Rathje, M. Grande, D. Hall, K. Kecsuemety, S. McKenna-Lawlor, K. Mursula, P. Tanskanen, Z. Pu, I. Sandahl, E. T. Sarris, M. Scholer, M. Schulz, F. Sorass, and S. Ullaland. RAPID - The Imaging Energetic Particle Spectrometer on Cluster. *Space Sci. Rev.*, 79:399–473, January 1997.

52. L. J. C. Woolliscroft, H. S. C. Alleyne, C. M. Dunford, A. Sumner, J. A. Thompson, S. N. Walker, K. H. Yearby, A. Buckley, S. Chapman, and M. P. Gough. The Digital Wave-Processing Experiment on Cluster. *Space Sci. Rev.*, 79:209–231, January 1997.

53. H.D. Young, R.A. Freedman, and A.L. Ford. *Sears and Zemansky's University Physics*. Pearson/Addison Wesley, 2004.

54. Y. Zhang, H. Matsumoto, and H. Kojima. Whistler mode waves in the magnetotail. *J. Geophys. Res.*, 104:28633–28644, 1999.

Mapping HF waves in the reconnection diffusion region

H. Viberg,[1] Yu. V. Khotyaintsev,[1] A. Vaivads,[1] M. André,[1] and J. S. Pickett[2]

Received 13 January 2013; revised 6 February 2013; accepted 6 February 2013; published 27 March 2013.

[1] We study in detail high-frequency (HF) plasma waves between the electron cyclotron and plasma frequencies within a reconnection diffusion region (DR) encountered by Cluster in the magnetotail using continuous electric field waveforms. We identify three wave types, all observed within the separatrix regions: Langmuir waves (LW), electrostatic solitary waves (ESWs), and electron cyclotron waves (ECWs). This is the first time the ECWs have been observed inside this region. Direct comparison between waveforms and electron distributions are made at the timescale of one energy sweep of the electron detector (125 ms). Based on the wave and electron distribution characteristics, we find that the separatrix region has a stratified spatial structure. The outer part of the region is dominated by LW emissions related to suprathermal electron beams propagating away from the X-line. Furthest in, nearest to the current sheet, we observe ESWs associated with counterstreaming electron populations. Studying HF waveforms allows for a precise mapping of kinetic boundaries in the reconnection region and helps to improve our understanding of the electron dynamics in the DR. **Citation:** Viberg, H., Yu. V. Khotyaintsev, A. Vaivads, M. André, and J. S. Pickett (2013), Mapping HF waves in the reconnection diffusion region, *Geophys. Res. Lett.*, *40*, 1032–1037, doi:10.1002/grl.50227.

1. Introduction

[2] Waves play an important role in the reconnection process [*Vaivads et al.*, 2006; *Fujimoto et al.*, 2011]. Scattering of particles by plasma waves can support anomalous resistivity, which is needed for merging of field lines in collisionless plasmas. Wave generation leads to relaxation of steep gradients in plasma parameters and strong currents, and thus observation of a particular wave mode provides insight into details of the particle distribution functions generating the wave, which can be otherwise difficult to resolve using particle instruments.

[3] Various types of HF waves have been observed in situ in relation to reconnection. Electrostatic solitary waves (ESWs) were observed in the reconnection regions in the magnetotail [*Deng et al.*, 2004; *Cattell et al.*, 2005; *Khotyaintsev et al.*, 2010] and at the magnetopause [*Retinò et al.*, 2006]. Langmuir waves (LWs) have been observed in the reconnection regions in the magnetotail [*Farrell et al.*, 2002], at the magnetopause [*Vaivads et al.*, 2004], and in the exterior cusp [*Khotyaintsev et al.*, 2004]. *Vaivads et al.* [2006] speculated that electron cyclotron waves (ECWs) can also be generated in the reconnection regions by transverse electron temperature anisotropies or loss cone distributions; however, no observations of such waves have been reported. HF waves are generated by unstable electron distributions and thus provide detailed information about the electron-scale dynamics. As fields can be sampled at much higher cadences than the particle distributions, the wave observations can potentially provide the highest possible resolution diagnostics of the electron-scale processes in the reconnection regions. However, this requires detailed understanding of the relation between the different types of waves and electron distributions produced throughout the reconnection region, and, despite numerous reports of HF waves, such a relation is still only partially established.

[4] In this letter, we present detailed in situ observations of electrostatic HF waves and related electron distributions inside the reconnection diffusion region (DR). We map observations of different wave types to different parts within this region and discuss possible generation mechanisms.

2. Observations

[5] We present an observation of a reconnection DR encountered by four Cluster spacecraft (S/C) at $[-19, 2.1, 0.7]R_E$ (GSM) on 10 September 2001, during southward interplanetary magnetic field (IMF). We use data from C1, C3, and C4. Magnetic field data are acquired using the fluxgate magnetometer (FGM) instrument [*Balogh et al.*, 1997]. For ion and electron data, we use the Cluster Ion Spectrometry (CIS) [*Reme et al.*, 1997] and plasma electron and current experiment (PEACE) [*Johnstone et al.*, 1997] instruments, respectively. The HF waveforms are measured by the cluster wide band data (WBD) [*Gurnett et al.*, 1997] instrument. For the entire event, the WBD instrument continuously samples the electric field waveform at 27.4 kHz, covering the electron plasma frequency, $f_{pe} \lesssim 10$ kHz.

[6] Figure 1 shows an overview of a DR crossing observed by C4. This interval has been identified as a reconnection DR by *Eastwood et al.* [2010]. The reconnecting component of B, B_x, is positive throughout the event (Figure 1a), except for a short interval between 08:01:30 UT and 08:03:00 UT, consistent with the S/C being located north of the current sheet (CS) most of the time. A reversal of ion flow from tailward to earthward (v_x in Figure 1b) is observed between 07:56:10 UT and 07:57:45 UT, which can be interpreted as a reconnection X-line passing the S/C in the tailward direction. Consistent with this, during the flow reversal the component of B normal to the CS (B_z in Figure 1a) changes sign from southward to northward. Simultaneously, the component along the current direction, B_y, changes from –10 nT to +10 nT, consistent with a crossing of the Hall quadrupole field structure north of the CS [see, e.g., *Vaivads et al.*, 2004].

[1]Swedish Institute of Space Physics, Uppsala, Sweden.
[2]Department of Physics and Astronomy, The University of Iowa, Iowa City, IA, USA.

Corresponding author: H. Viberg, Swedish Institute of Space Physics, Uppsala, Sweden. (henrik.viberg@irfu.se)

0094-8276/13/10.1002/grl.50227

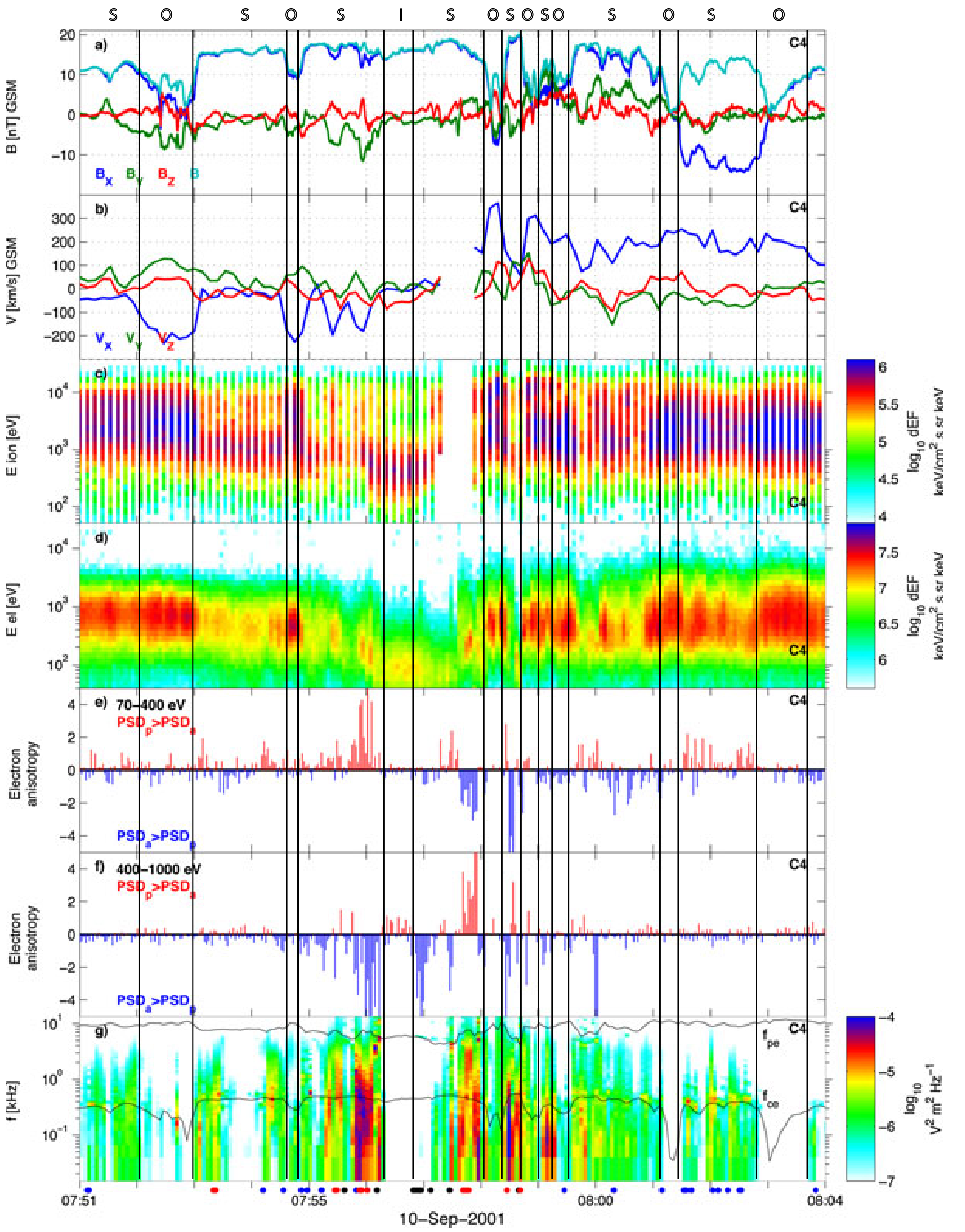

Figure 1. Overview of the DR encounter by Cluster 4, on 10 September 2001. (a) Magnetic field from FGM, (b) ion velocities (CIS), (c) ion spectrogram (CIS), (d) electron spectrogram (PEACE), (e and f) electron anisotropy (PEACE), and (g) wave spectrum with sampling frequency 27.4 kHz (WBD). The electron plasma frequency (f_{pe}, computed from the electron density measured by PEACE) and electron cyclotron frequency (f_{ce}, computed from FGM data) are plotted in Figure 1g as solid black lines. The colored dots at the bottom of Figure 1g indicate the times when ECW (blue), ESW (red), and LWs (black) are detected.

[7] Cluster encounters several regions with different plasma characteristics within the DR. The exhaust (ion outflow, labeled "O") regions are characterized by $|v_x| > 100$ km/s (Figure 1b) and $B_x < 10$ nT. There we observe the plasma sheet ($T_e \sim 1$ keV) plasma with flat-top electron distributions [*Asano et al.*, 2008]. At the flow reversal, an inflow region is observed (labeled "I"). It is characterized by v_z of several tens of kilometers per second in the negative z-direction (inflow of plasma into the CS), near-zero v_x, and large B_x. The inflow is populated with the cold lobe plasma ($T_e \sim 100$ eV); the electron distributions are mostly anisotropic, with parallel pressure exceeding the perpendicular one, similar to observations at the magnetopause [*Egedal et al.*, 2011]. Between the outflow and inflow regions are the separatrix regions (SR) [*Khotyaintsev et al.*, 2006; *Lindstedt et al.*, 2009], labeled "S." The SR are populated with a mix of plasma sheet and lobe plasmas; the electron distributions are anisotropic. To characterize the anisotropy, we introduce anisotropy factor α: $\alpha = 1 - (PSD_a/PSD_p)$ for $PSD_p < PSD_a$, and $\alpha = (PSD_p/PSD_a) - 1$ for $PSD_p > PSD_a$, where PSD_p and PSD_a denote the electron phase space densities in the parallel and antiparallel to

B directions, respectively. So that for $\alpha > 0 (\alpha < 0)$, the parallel to B electron flux is higher (lower) than the antiparallel. We plot α for two energy bands: 70–400 eV (lobe, Figure 1e) and 400–1000 eV (plasma sheet, Figure 1f). The largest anisotropy is localized in the SR close to the flow reversal and that α has opposite signs for the high- and low-energy bands consistent with low (high)-energy electrons flowing towards (away from) the X-line.

[8] Figure 1g shows an electric field spectrogram in a frequency range 0.02–13.5 kHz which contains the electron cyclotron frequency, f_{ce}, and the electron plasma frequency, f_{pe}. Most of the wave power is concentrated in the SR with the highest amplitude waves localized within ±3 min around the flow reversal. Figure 2a shows a detailed spectrogram for a part of the SR between 07:56:00 and 07:56:16 UT illustrating the three main types of the wave emissions observed: narrowband emissions at f_{ce} and f_{pe} and broadband emissions. Using the fact that the angle between B and the electric field boom (EFW p12) is changing with the S/C spin, we investigate the polarization of the electric field for the different types of emissions. We find that E is primarily perpendicular to B for the narrowband emissions at f_{ce}, and parallel to B for the other two types. Therefore, we identify the three types of emissions as ECWs, LWs, and ESWs. Figures 2b–2d show typical examples of waveforms and spectra for the three emission types, as well as the electron distributions associated with them; the presented waveforms are sampled during 125 ms-long intervals of the PEACE energy sweep. The ECWs, $E_\perp \gg E_\parallel$, have a sharp peak at f_{ce}, 2 orders of magnitude larger than the signal below f_{ce} (Figure 2b). For the LWs, $E_\parallel \gg E_\perp$, the waveform has a distinct beat-like shape, and the spectrum has a sharp peak at f_{pe} (Figure 2c). The beating could originate from nonlinear wave-wave interactions [*Khotyaintsev et al.*, 2001], or a linear process whereby electron beams in the presence of density inhomogeneities generate several Langmuir modes at different frequencies, which mix to form the modulation [*LaBelle et al.*, 2010]. ESWs (Figure 2d) are bipolar pulses of $E_\parallel$ with a corresponding broadband spectrum [*Matsumoto et al.*, 1994].

[9] We have analyzed waveforms for all 125 ms-long intervals of PEACE measurements (2 times per ~4 s S/C spin) for the time intervals presented in Figure 1. To compare the waveforms and the electron distributions, we select only the cases where the waveforms show similar characteristics during the whole PEACE energy sweep. Typically one type of waveform can be observed for up to 10 s (see for example Figure 2a); however, the ECWs usually have a shorter characteristic timescale, with some of the shortest waveforms being only 50 ms long. Also, we have selected only the high-amplitude waves for which the wave power exceeds a certain amplitude threshold (different for the different wave types). This resulted in a data set of 50+ intervals of each of the three emission types for all three Cluster S/C with WBD data available. The examples presented in Figure 2 are some typical examples selected from this data set. The intervals with different emission types for C4 are marked in the bottom of Figure 1g. One can see that the LWs and ESWs are related to strongly anisotropic electron distributions detected around the flow reversal, with the LWs being related to a beam-like distribution (Figure 2c, panel 3) and ESWs to counterstreaming distributions (Figure 2d, panel 3). The electron distributions observed with ECWs do not show strong anisotropies (see for example Figure 2b, panel 3). However, the electron measurements at lower energies are strongly affected by photoelectrons emitted by the EFW probes, and we cannot exclude the possible presence of cold electron beams or shell-type distributions.

3. Discussion

[10] To put the wave observations into the reconnection context, we draw the approximate paths of C1, C3, and C4 (no WBD data on C2) together with a sketch of the reconnection DR (Figure 3b). The positions of the Cluster S/C in the GSM X–Z plane are shown in Figure 3a. The S/C are first located in the tailward flow and then enter the earthward flow. C1 and C4 are north of the CS, at approximately the same distance from the center, and C3 is south of the CS and somewhat closer to the center than C1 and C4, as C3 observes the exhaust most of the time. The waves are almost exclusively localized in the SRs (initially determined from the particle data), which are encountered multiple times. Similar to magnetopause observations of *Retinò et al.* [2006], statistically the order in which the different wave types are observed suggests a spatially stratified SR:

[11] *Inflow.* The electron fluxes parallel and antiparallel to B are equal, the distribution is stable, and no waves are observed. Electron pressure anisotropy is developing with approach towards the electron DR [*Egedal et al.*, 2011].

[12] *Outer SR.* With the crossing of the separatrix (electron edge), the first electrons coming from the X-line arrive. These electrons will be seen as a suprathermal low density beam due to the acceleration at the X-line and the time-of-flight effect (most energetic electrons are expected closer to the inflow boundary). Such an electron distribution can be unstable to the bump-on-tail instability generating LWs [*Omura et al.*, 1996]. This expectation is consistent with the observed LWs, which are primarily detected in the outer part of the SR (closest to the inflow). Also the electron distributions observed with the LWs show presence of a suprathermal beam. Moreover, at all the crossings of the boundary between the inflow and the SR, the LWs are the first waves detected; therefore, such waves are a signature of the separatrix (electron edge).

[13] *Inner SR.* Deeper inside the SR, the density of the beam electrons moving away from the X-line increases, and also the background population carrying the Hall current experiences a significant net drift towards the X-line. Such a distribution can set up two-stream and Buneman instabilities generating ESWs [*Omura et al.*, 1994, 1996; *Markidis et al.*, 2012; *Divin et al.*, 2012]. We observe the ESWs deeper in the SR and in relation to counterstreaming low- and high-energy electron populations.

[14] *Ion outflow.* In the ion outflow regions, rather isotropic electron distributions which are stable to wave generation are expected. This is consistent with observed flat-top shaped distributions and little or no wave activity.

[15] Figure 2a shows an example of a SR crossing illustrating the proposed stratified structure of the region. In the beginning of the interval, C4 is in the inner part of the region and detects ESWs. Then it moves to the outer part with LWs, and then finally wave activity ceases, marking the crossing of the separatrix (electron edge) and transition to the inflow region. The boundary to the outflow can be nicely seen in

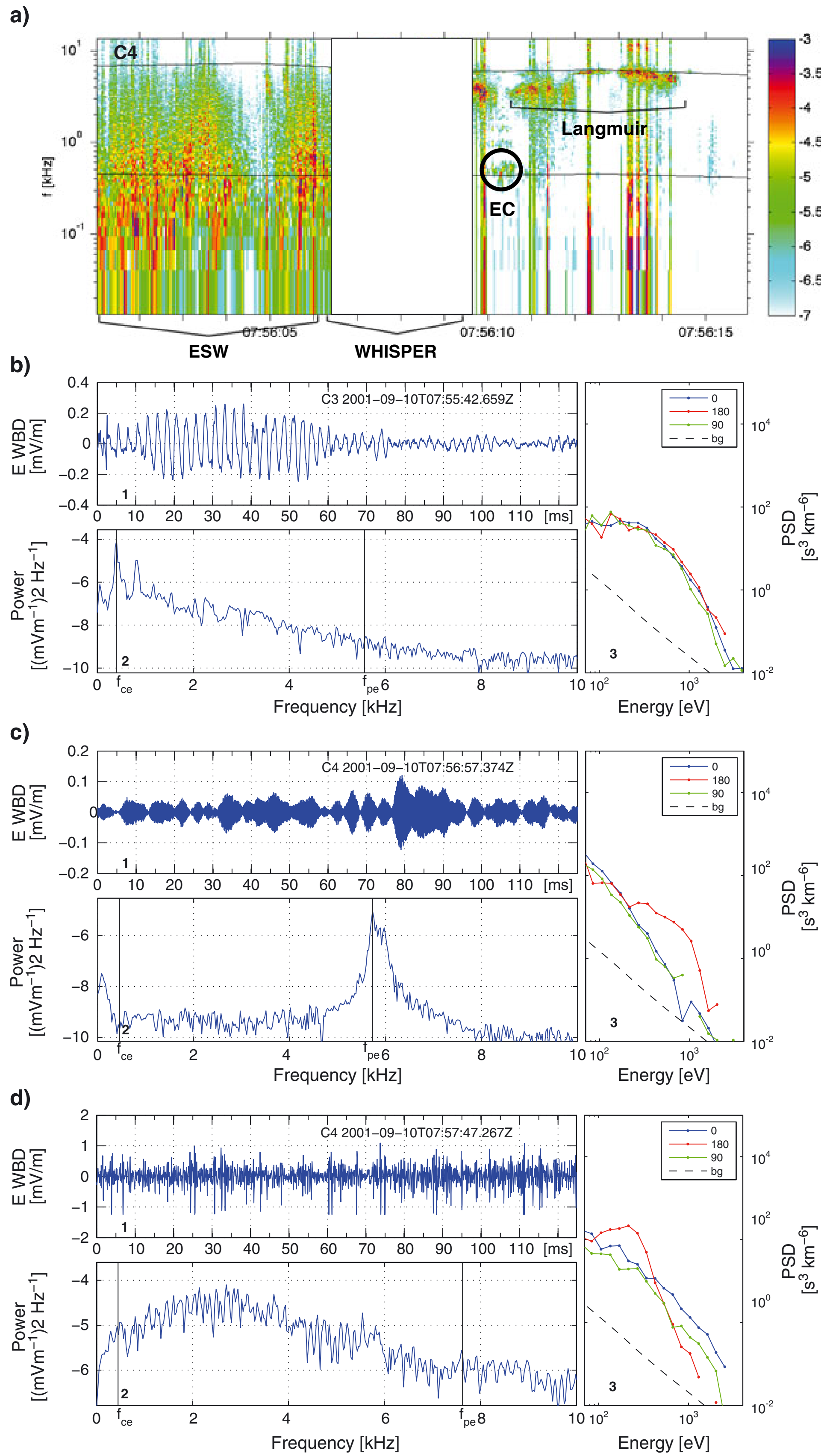

Figure 2. (a) An example of a SR crossing, (b) an EC wave, (c) a LW, and (d) ESWs. The panels show (1) waveform observed simultaneously with the electron distribution (time in milliseconds after start of PEACE sweep), (2) the spectrum of the waveform, with f_{ce} and f_{pe} marked, and (3) the electron phase space density, corrected for the S/C potential and measured at 0°, 90°, and 180°. The dashed line shows the one-count level of the instrument.

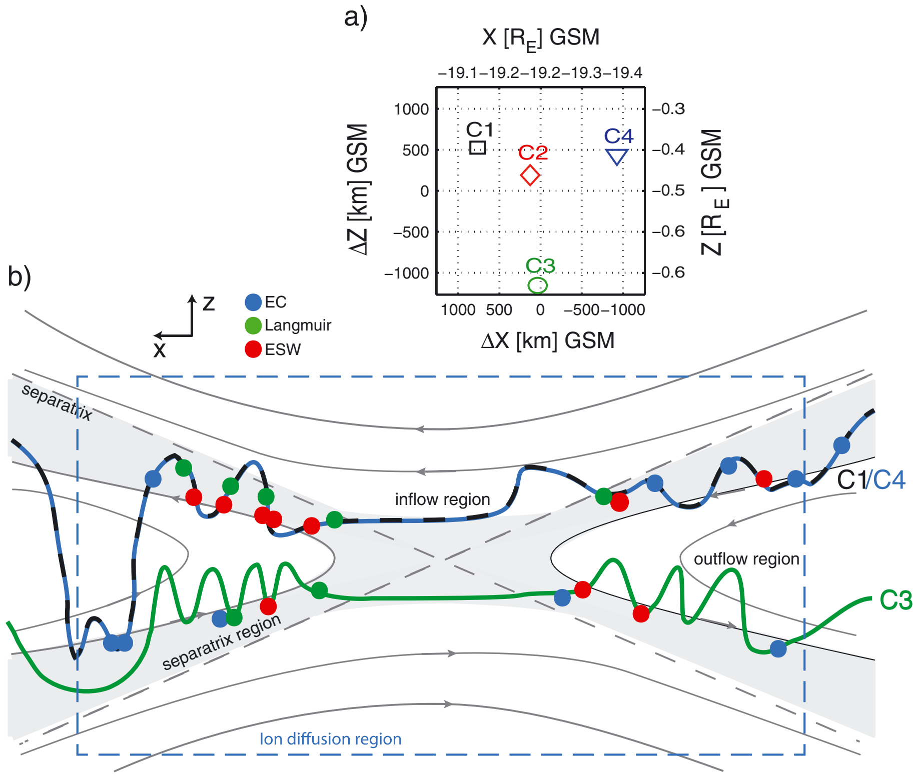

Figure 3. Sketch of the event, with (a) the positions of the Cluster S/C and (b) the reconnection DR, with the approximate paths of C1, C3, and C4. Wave observations are indicated by the colored dots, and the different regions within the DR (blue box) are labeled.

Figure 1g at 8:01:10 and 8:01:30 UT when C4 crosses the center of the exhaust ($B_x = 0$) and the wave activity ceases.

[16] We present the first observations of the ECWs in the reconnection DR. The ECWs are observed at different locations in the SR, with some tendency to be farther away from the flow reversal than LWs and ESWs. Rather isotropic distributions similar to flat-top are observed together with the ECWs; however, we are unable to fully resolve the low-energy part of the electron distribution and thus cannot rule out the presence of low-energy electron beams and shell-like distributions. The observed ECWs are very bursty, with the shortest wave packets lasting only for several tens of electron gyroperiods ($f_{ce} \sim 0.5$ kHz), which indicates that the instability driving the wave is rather strong. *Vaivads et al.* [2006] speculated that ECWs can be generated in the DR by, for example, unstable shell/loss cone [*Sundkvist et al.*, 2006] or beam distributions [*Menietti et al.*, 2002]. The ECWs can be responsible for isotropization of shell distributions (forming flat-tops) which are formed as electron beams enter regions with increasing B. Rapid increase of B is expected, for example, in the flux pileup region leading to, among others, generation of whistlers [*Fujimoto and Sydora*, 2008; *Khotyaintsev et al.*, 2011], as well as at the separatrices in the vicinity of the X-line. At the moment, there is no clear picture of ECW generation in the DR, and this problem requires further investigation by simulations.

[17] We present a detailed comparison of waves and electron distribution obtained at very short periods of time compared to previous studies of HF waves in magnetotail reconnection [*Farrell et al.*, 2002; *Deng et al.*, 2004], and most importantly, we compare simultaneous wave and electron measurements at timescales of one energy sweep of the electron detector. A similar study of HF waveforms and sub-spin electron data has been performed by *Retinò et al*. [2006] at the magnetopause SR. For the magnetotail case presented here, the typical plasma scales are a factor of 10 larger than for the magnetopause, and also, the S/C observe the DR for a significantly longer period. These factors combined with multi-S/C observations allow us to collect a sufficiently larger data set of wave observations and draw a "statistical" picture of the distribution of the waves in the ion DR.

4. Conclusions

[18] We presented detailed multi-spacecraft observations of high-frequency (HF) electrostatic waves in a frequency range containing f_{ce} and f_{pe} and related electron distributions in the reconnection diffusion region (DR) which is encountered by the Cluster S/C separated by several ion scales in the terrestrial magnetotail. We used the high-resolution electric field waveforms continuously sampled by WBD throughout the DR by three of the Cluster S/C.

[19] We have identified the three main types of the HF emissions in the DR as Langmuir waves (LWs), electrostatic solitary waves (ESWs), and electron cyclotron (EC) waves, which are reported for the first time. In order to study the relation of the different waveforms to electron distributions, we compare the waveforms with electron distributions measured at timescales of one energy sweep of the electron detector (125 ms), as the observed waveforms are rapidly changing on timescales of the order of seconds. As we have measurements on three Cluster S/C and the S/C spend

several minutes in the DR, we are able to collect a large data set of waveforms and corresponding electron distributions.

[20] We find little or no activity in the inflow and outflow regions, and most of the wave activity is localized to the separatrix regions (SR), which are crossed multiple times by Cluster. From the multiple crossings of the separatrix region, we find that it has a spatially stratified structure. In the outer part of the region (closest to the inflow), the LWs are observed, generated by suprathermal low density electron beams propagating away from the *X*-line, and thus, the appearance of the first LWs when the S/C is entering the DR from the inflow is a signature of the separatrix (electron edge). In the inner part of the SR, mostly ESWs are observed together with electron distributions showing counterstreaming electron populations (low-energy towards the *X*-line, high-energy away from the *X*-line). EC waves are observed in different parts of the SR; they have the shortest timescales of the three observed wave types (down to several tens of milliseconds or several tens of electron gyroperiods), which possibly reflects fast relaxation of perpendicular electron anisotropies created in the DR. There is also a rather distinct boundary seen in waves between the SR and the central part of the exhaust, where no waves are observed.

[21] We provide new and important information concerning the properties and locations of HF waves and electron dynamics in the reconnection DR and provide a precise mapping of the kinetic boundaries. Improved particle instrumentation, such as provided by the upcoming MMS mission, would allow us to study the electron dynamics at the *X*-line in even greater detail.

[22] **Acknowledgments.** We thank the ESA Cluster Active Archive for providing the data for this study. This research is supported by the Swedish National Space Board and the Swedish Research Council under grants 2007-4377, 2009-3902, and 2009-4165. J.S.P. acknowledges support from NASA GSFC under Grant NNX11AB38G.

References

Asano, Y., et al. (2008), Electron flat-top distributions around the magnetic reconnection region, *J. Geophys. Res.*, *113*, A01207, doi: 10.1029/2007JA012461.

Balogh, A., et al. (1997), The Cluster magnetic field investigation, *Space Sci. Rev.*, *79*, 65–91, doi:10.1023/A:1004970907748.

Cattell, C., et al. (2005), Cluster observations of electron holes in association with magnetotail reconnection and comparison to simulations, *J. Geophys. Res.*, *110*, A01211, doi:10.1029/2004JA010519.

Deng, X. H., et al. (2004), Geotail encounter with reconnection diffusion region in the Earth's magnetotail: Evidence of multiple *X* lines collisionless reconnection? *J. Geophys. Res.*, *109*, A05206, doi: 10.1029/2003JA010031.

Divin, A., et al. (2012), Numerical simulations of separatrix instabilities in collisionless magnetic reconnection, *Phys. Plasmas*, *19*, 042110, doi: 10.1063/1.3698621.

Eastwood, J. P., T. D. Phan, M. Øieroset, and M. A. Shay (2010), Average properties of the magnetic reconnection ion diffusion region in the Earth's magnetotail: The 2001–2005 Cluster observations and comparison with simulations, *J. Geophys. Res.*, *115*, A08215, doi: 10.1029/2009JA014962.

Egedal, J., A. Le, P. L. Pritchett, and W. Daughton (2011), Electron dynamics in two-dimensional asymmetric anti-parallel reconnection, *Phys. Plasmas*, *18*, 102901, doi:10.1063/1.3646316.

Farrell, W. M., et al. (2002), The dominance of electron plasma waves near a reconnection *X*-line region, *Geophys. Res. Lett*, *29*, 1902, doi: 10.1029/2002GL014662.

Fujimoto, K., and R. D. Sydora (2008), Whistler waves associated with magnetic reconnection, *Geophys. Res. Lett.*, *35*, L19112, doi: 10.1029/2008GL035201.

Fujimoto, M., I. Shinohara, and H. Kojima (2011), Reconnection and waves: A review with a perspective, *Space Sci. Rev.*, *160*, 123–143, doi: 10.1007/s11214-011-9807-7.

Gurnett, D. A., R. L. Huff, and D. L. Kirchner (1997), The Wide-Band Plasma Wave Investigation, *Space Sci. Rev.*, *79*, 195–208, doi: 10.1023/A:1004966823678.

Johnstone, A. D., et al. (1997), Peace: A Plasma Electron and Current Experiment, *Space Sci. Rev.*, *79*, 351–398, doi: 10.1023/A: 1004938001388.

Khotyaintsev, Y, G. Lizunov, and K. Stasiewicz (2001), Langmuir wave structures registered by FREJA: Analysis and modeling, *Adv. Space Res.*, *28*, 1649–1654, doi:10.1016/S0273-1177(01)00485-9.

Khotyaintsev, Y., et al. (2004), Cluster observations of HF waves in the exterior cusp, *Ann. Geophys.*, *22*, 2403–2411, doi:10.5194/angeo-22-2403-2004.

Khotyaintsev, Y. V., et al. (2006), Formation of inner structure of a reconnection separatrix region, *Phys. Rev. Lett.*, *97*, 205003, doi: 10.1103/PhysRevLett.97.205003.

Khotyaintsev, Y. V., et al. (2010), Observations of slow electron holes at a magnetic reconnection site, *Phys. Rev. Lett.*, *105*, 165002, doi: 10.1103/PhysRevLett.105.165002.

Khotyaintsev, Y. V., et al. (2011), Plasma jet braking: Energy dissipation and nonadiabatic electrons, *Phys. Rev. Lett.*, *106*, 165001, doi: 10.1103/PhysRevLett.106.165001.

LaBelle, J., I. H. Cairns, and C. A. Kletzing (2010), Electric field statistics and modulation characteristics of bursty Langmuir waves observed in the cusp, *J. Geophys. Res.*, *115*, A10317, doi:10.1029/2010JA015277.

Lindstedt, T., et al. (2009), Separatrix regions of magnetic reconnection at the magnetopause, *Ann. Geophys.*, *27*, 4039–4056, doi:10.5194/angeo-27-4039-2009.

Markidis, S., et al. (2012), Three dimensional density cavities in guide field collisionless magnetic reconnection, *Phys. Plasmas*, *19*, 032119, doi: 10.1063/1.3697976.

Matsumoto, H., et al. (1994), Electrostatic solitary waves (ESW) in the magnetotail: BEN wave forms observed by GEOTAIL, *Geophys. Res. Lett.*, *21*, 2915–2918, doi:10.1029/94GL01284.

Menietti, J. D., O. Santolik, J. D. Scudder, J. S. Pickett, and D. A. Gurnett (2002), Electrostatic electron cyclotron waves generated by low-energy electron beams, *J. Geophys. Res.*, *107*, 1285, doi: 10.1029/2001JA009223.

Omura, Y., H. Kojima, and H. Matsumoto (1994), Computer simulation of electrostatic solitary waves: A nonlinear model of broadband electrostatic noise, *Geophys. Res. Lett.*, *21*, 2923–2926, doi: 10.1029/94GL01605.

Omura, Y., H. Matsumoto, T. Miyake, and H. Kojima (1996), Electron beam instabilities as generation mechanism of electrostatic solitary waves in the magnetotail, *J. Geophys. Res.*, *101*, 2685–2698, doi: 10.1029/95JA03145.

Reme, H., et al. (1997), The Cluster Ion Spectrometry (CIS) experiment, *Space Sci. Rev.*, *79*, 303–350, doi:10.1023/A:1004929816409.

Retinò, A., et al. (2006), Structure of the separatrix region close to a magnetic reconnection X-line: Cluster observations, *Geophys. Res. Lett.*, *33*, L06101, doi:10.1029/2005GL024650.

Sundkvist, D., et al. (2006), Shell-instability generated waves by low energy electrons on converging magnetic field lines, *Geophys. Res. Lett.*, *33*, L03103, doi:10.1029/2005GL024388.

Vaivads, A., et al. (2004), Structure of the magnetic reconnection diffusion region from four-spacecraft observations, *Phys. Rev. Lett.*, *93*, 105001, doi:10.1103/PhysRevLett.93.105001.

Vaivads, A., et al. (2006), Plasma waves near reconnection sites, In: *Geospace Electromagnetic Waves and Radiation,* edited by J. W. Labelle & R. A. Treumann, vol. 687 of Lect. Notes Phys., Berlin Springer Verlag, 251.

Whistler Mode Waves at Magnetotail Dipolarization Fronts

H. Viberg,[1,2] Yu. V. Khotyaintsev,[1] A. Vaivads,[1], M. André[1], H. S. Fu[3], and N. Cornilleau-Wehrlin[4,5]

Dipolarization fronts (DFs) are commonly observed in the magnetotail, as the front of the reconnection jets. The statistics of whistler waves around DFs in the Earth's magnetotail is studied. Using data from the Cluster spacecraft spanning a period of 9 years, 2001-2009, DFs are identified by fitting the z-component (GSM) of the magnetic field to a hyperbolic tangent function. We show that whistler mode waves are common at DFs; between 30-60 % of all DFs are associated with whistlers. It is also found that whistlers are about 20-40 times more likely to be observed at a DF than at any random location in the magnetotail. The distribution of whistlers at DFs is approximately independent of the distance from the Earth, along the X_{GSM} axis, between -20 and -10 R_E. The whistler waves are more common directly after the DF than before. The median frequency of the whistlers was $0.16f_{ce}$, with 75% being below $0.29f_{ce}$. Our results show that whistlers are characteristic signatures of DFs, and can be used to detect DFs when other types of measurements may not be available, e.g. on planetary missions.

1. Introduction

Dipolarization fronts, DFs, are tangential discontinuities in the magnetotail, separating the plasma sheet and reconnection jets[Fu et al., 2012b]. DFs are identified by a sharp gradient of the background magnetic field and are associated with fast plasma flows [Fu et al., 2012c; Liang et al., 2012], particle energization [Fu et al., 2012a; Asano et al., 2010] and can be produced by unsteady magnetic reconnection [Sitnov et al., 2009]. Runov et al. [2009] showed that DF evolution can be observed over large distances. DFs are also associated with various wave activities, e.g. electron holes, whistler, lower hybrid and electron cyclotron waves [Hwang et al., 2011; Le Contel et al., 2009; Sergeev et al., 2009; Zhou et al., 2009].

Whistler mode waves are right-hand circularly polarized electromagnetic waves with frequencies ranging from above the lower-hybrid frequency, f_{LH}, to below the electron cyclotron frequency, f_{ce} and are commonly observed in the magnetotail [Zhang et al., 1999; Liang et al., 2012]. Whistler waves typically lie in a frequency range from 0.1 to 0.6 f_{ce}, and have a mean amplitude of 1% of the background magnetic field. Bursts of whistler activities are often observed in connection with fast plasma flows [Liang et al., 2012].

A number of case studies [Le Contel et al., 2009; Deng et al., 2010; Khotyaintsev et al., 2011; Huang et al., 2012] reported observations of whistler waves in relation to DFs. In particular, they found whistlers in the magnetic flux pile-up region (FPR), where the electron distribution has a perpendicular anisotropy, which is large enough to drive whistler waves via the whistler anisotropy instability [Le Contel et al., 2009]. Le Contel et al. [2009] also showed that the bandwidth of the whistler signal correlated with the anisotropy, i.e. higher anisotropy is associated with a larger bandwidth, and that the electron anisotropy decreases away from the equator, ao that the waves have a higher growth rate closer to the equator. Using data from four Cluster spacecraft, Khotyaintsev et al. [2011] shows that the generation region is located at the equator. They suggested that whistler waves provide evidence of betatron heating in the FPR, which creates a temperature anisotropy $T_\perp > T_\parallel$. Whistlers efficiently scatter resonant electrons (energies close to thermal energies) in pitch angle, making the electron distribution more isotropic.

Despite existing case studies, the statistical relation between DFs and whistlers has not been established. If such a relation exists, it could be used as a signature of DF/transient reconnection in the magnetosphere. Planetary missions usually do not have particle data of sufficient resolution, so wave observations can then be used instead to infer the presence of DFs. In this letter we present statistics of whistler waves in relation to DFs observed by Cluster during 2001-2009.

2. Event study

Figure 1 shows an example of a whistler wave event behind a DF. In this event, the SC are located at $(-13, 8, -0.2)R_E$ GSM. The DF is clearly seen as a sharp increase of B_z (panel a). The electron density (panel b) decreases at the DF. Panel c shows the x-component of the ion velocities, using both data from the CIS-HIA instrument (blue) and the calculated $v_{E\times B}$ velocity, lowpass filtered between 0 and 10 Hz (black). We see that v_x increases in the FPR, up to a maximum of 450 km/s. The velocity peak is located behind the DF, so in this case we are observing a growing flux pile-up region [Fu et al., 2011].

Panel d shows the electron differential energy flux (DEF) from PEACE, averaged over pitch angle. In the FPR, the temperature of the electron population increases from about 3 keV to 5 keV. After this, the temperature drops to the same value as before. The pitch angle distribution is displayed in panel e for energies between 3 to 10 keV. As can be seen, the distribution is mostly isotropic up until the DF, where the perpendicular flux increases, corresponding to $T_\perp > T_\parallel$. This is a sign of betatron acceleration at the DF caused by the sharp increase of the magnetic field.

In the FPR, where the electron distribution has high perpendicular anisotropy, we observe an increase of the power spectral density (PSD) of the wave magnetic field (panel f).

[1]Swedish Institute of Space Physics, Uppsala, Sweden.
[2]Uppsala University, Department of Physics and Astronomy, Uppsala, Sweden.
[3]Space Science Institute, School of Astronautics, Beihang University, Beijing, China.
[4]LPP, Ecole Polytechnique, CNRS, Palaiseau, France.
[5]LESIA, Observatoire de Paris, Meudon, France.

0094-8276/13/$5.00

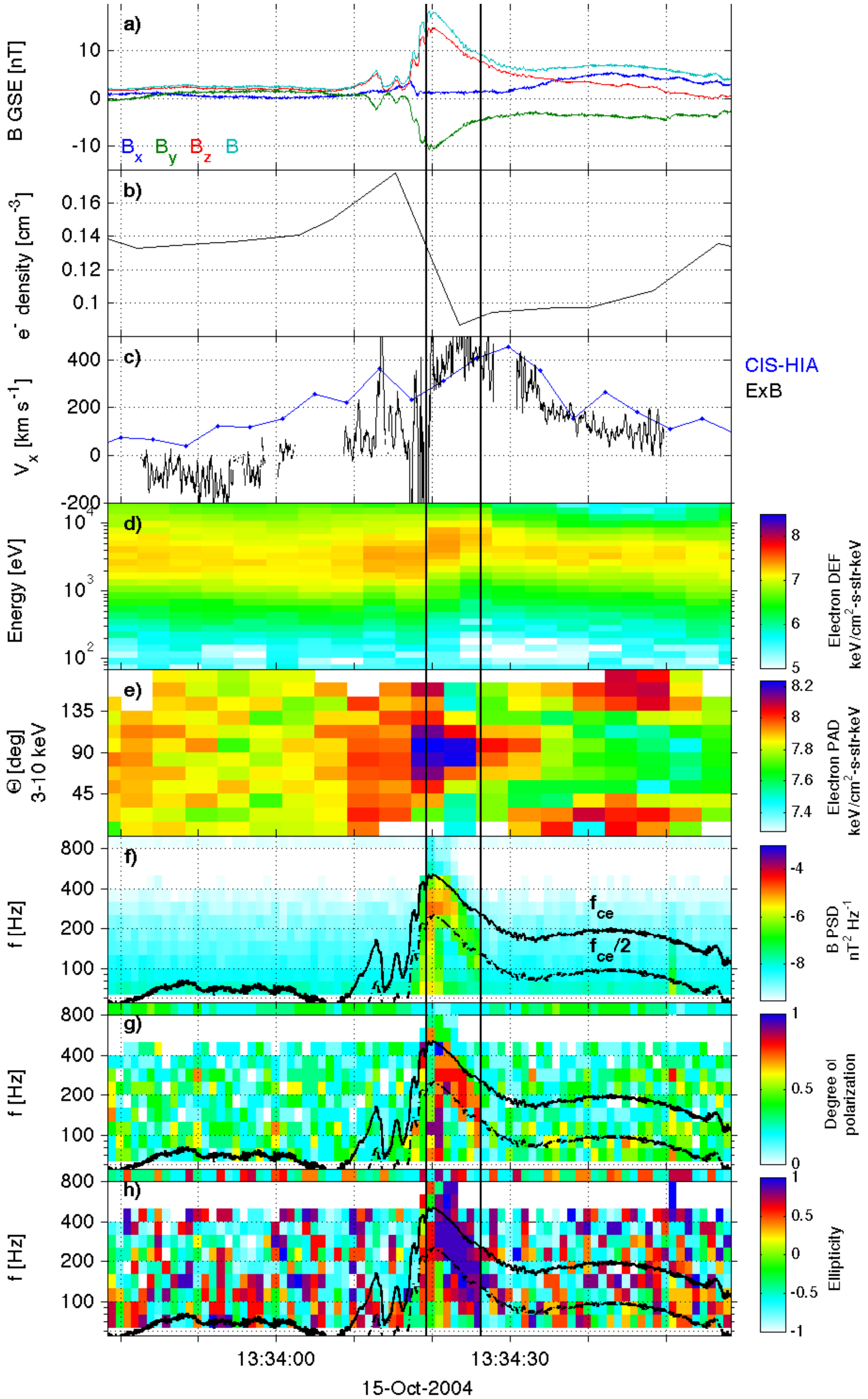

Figure 1. Overview a DF event observed by C1. From top to bottom: a) magnetic field from FGM [Balogh et al., 2001], b) electron density from PEACE [Owen et al., 2001], c) ion velocity (X GSM) from both CIS [Rème et al., 2001] and v_{ExB} using EFW [Gustafsson et al., 2001], d) electron differential energy flux, e) pitch-angle distribution for energies of 3-10 keV, f) power spectral density of the wave magnetic field, g) the degree of polarization, and h) the ellipticity. Data for the last three panels are calculated from spectral matrices produced by on board STAFF Spectrum Analyser [Cornilleau-Wehrlin et al., 2003], using the PRASSADCO program [Santolík, 2000]. The black lines in panels f-h show f_{ce} and $0.5f_{ce}$, respectively. The black vertical lines mark the FPR, where the strongest waves are observed.

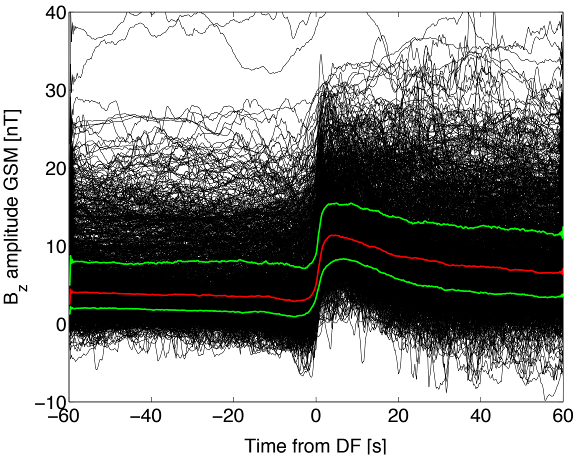

Figure 2. Superposed epoch of all DF events observed by the Cluster spacecraft. The red line shows the median B_z and the two green lines the 25th and 75th percentiles. The median jump in B_z is about 6.1 nT and the median duration of the DF is about 1.8 seconds.

The wave maximum activity is localized between f_{ce} and $0.5f_{ce}$ (marked by black lines). The duration of the wave burst is about 8 s. The median degree of polarization is ~ 0.7 and the median ellipticity is close to $+1$ for the whole burst (panels f and g). Such properties indicate that the wave belongs to the whistler mode. Although we present only data from C1 in Figure 1, the same wave structure was observed by all four SC in this specific event; the maximum inter-spacecraft separation was 1100 km in GSM-X.

3. Data selection and wave identification

Next, we perform a statistical analysis of whistler waves at DFs. Our study is done in two steps: first we search for DFs in the magnetotail and then, from the events obtained from step one, identify whistler waves.

3.1. DF observations

We use the DF search algorithm by Fu et al. [2012a], but extend the search to all four SC, for the tail periods from 2001 to 2009; the tail box is defined as having $-20 < X < -10\ R_E$, $-12 < Y < 12\ R_E$,and $-5 < Z < 5\ R_E$ (GSM). The DFs were identified by fitting a hyperbolic tangent function to B_z:

$$B_{fit} = \frac{a}{2}\tanh\left(\frac{\Delta t}{b/2}\right) + \left(c + \frac{a}{2}\right), \qquad (1)$$

where $\Delta t = t - t_{DF}$ is the time interval from 60 s before to 15 s after the DF. The fitting coefficients a, b, and c are obtained for each event and represent the jump in B_z, the duration of the DF, and the magnitude of B_z one minute before the DF, respectively.

We searched for DFs through all tail periods between 2001 and 2009 and found in total 1271 DF events, however several of these are the same DF, observed by multiple spacecraft. The number of DFs observed by only one SC is 608, 169 were detected by two, 63 by three, and 34 by four SC, giving a total of 873 unique DFs. A superposed plot of all DFs for the tail epoch is shown in Figure 2. The red line shows the median B_z and the two green lines show the 25th and 75th percentiles. We get a median jump of 6.1 nT and a median duration of 1.8 seconds. Our median flow velocity is 200 km s^{-1}. The ion inertial length of each DF is calculated from ion moments where CIS-data is available (C1, C3, C4). We get a median ion inertial length of about 565

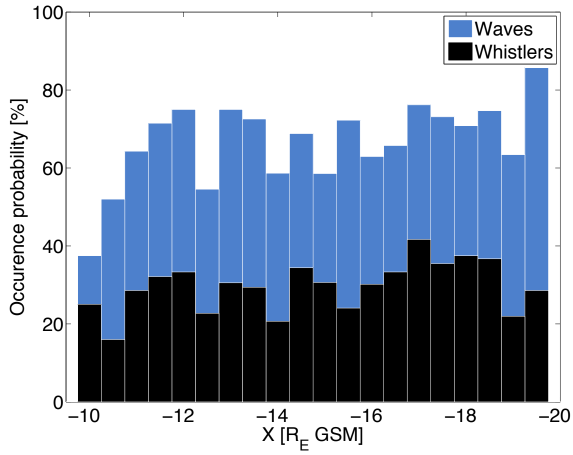

Figure 3. Distribution of waves and whistler waves in X (GSM). The height of the bar tells the ratio between the number of wave or whistler events, divided by the number of DF events, for each X bin. The blue bars show the occurence of any emission identified as a wave by our algorithm. The black bars show the occurence of those emissions that were classified as whistler waves. About 30 % of the DFs are associated with whistler waves, and about 60 % with general waves. Since our algorithm probably rejects many whistler waves, but accepts them as waves, the true whistler distribution would lie somewhere between the blue and black bars.

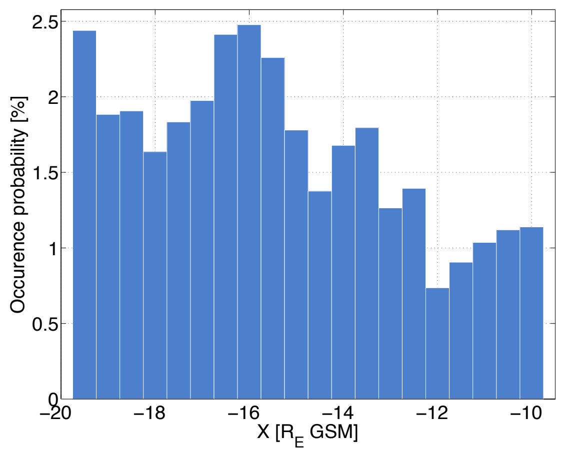

Figure 4. Occurence probability for finding whistlers anywhere in the tail box during the period from 2001-2009. The average probability is about 1.5%. This is a significantly lower probability than for finding a whistler at a DF.

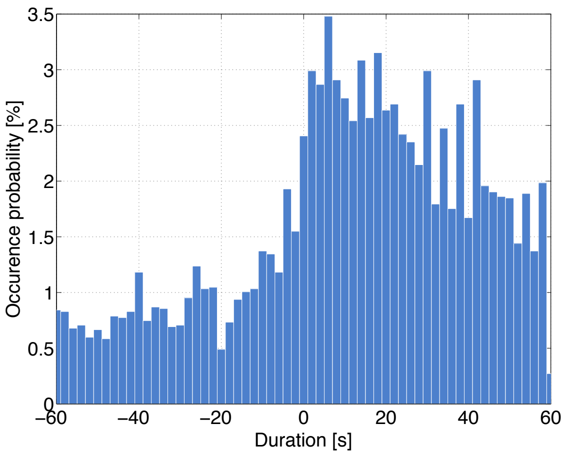

Figure 5. Histogram of the time between the DF observation and the whistler emission. The plot is centered around the time of the DF observation. The whistler waves are clearly more common at and after the DF than before. The probability begins to increase a few seconds before the DF.

km, which gives a median DF thickness of 0.64 ion inertial lengths. These results are consistent with Fu et al. [2012a].

3.2. Whistler wave identification

We search through the identified DF events for signs of whistler waves by gradually filtering out non-wave signals, in a way similar to Bortnik et al. [2007]. We shall call a point in the spectra of Figure 1 f-h a "pixel", defined as having a certain time duration (1s or 4s, depending on STAFF SA operation mode) and a certain width in frequency. The reason we use pixels is that the STAFF-PPP data is delivered as spectral arrays. For all recognized DF events, defined as the period ±60 seconds from the DF, we first remove any pixel in the magnetic field spectrum that is less than 10 times the median at that specific frequency. We then look, for each time step, for local maxima in frequency in the remaining data and keep the strongest maxima, and the pixels directly above and below. The next step is to keep the pixels that are continuous in time, with the requirement that a signal must be at least two pixels wide in time. After that, we also look at continuity in frequency, i.e. the pixels must connect to each other as a continuous group. The final step is to look at each group of pixels and keep only those that have a median ellipticity greater than 0.7.

After all this is done, we have a list of identified 2-minute DF events that contain whistler wave observations. We also keep a list of those events that exhibited general wave emissions, i.e. was sufficiently above median amplitude and had a distinct peak in the spectra, but did not necessarily have the required length or contiguity.

The method will most likely miss some whistler waves due to the search criteria. For example, a wave identified as having the strongest local maximum in frequency at a specific time may turn out to not have the desired ellipticity, and is then discarded. The second strongest peak of that event might have been a whistler wave. Using a certain number of pixels rather than a certain time to identify continuous wave signals is also likely to decrease the number of approved whistler events. Events lasting just a bit shorter than 8 s may be interpreted as only one data point in normal bit rate (time resolution 4 s). There are much more observations in normal bit rate than in high bit rate. Also, whistler emissions may be fragmented into many pieces, each shorter than two pixels, not fulfilling our criteria. Thus we get a conservative estimate of the occurence rate of whistlers versus waves at DFs.

4. Statistical results

Out of 1272 DF events, 859 were found to have wave emissions, and out of these we find 394 events that fulfilled the whistler criteria. The ratio of DFs that are associated with whistler waves is thus somewhere between 31% to 67%, see Figure 3. We note, however, that our DF detection algorithm is likely to miss many weaker fronts.

Since our algorithm has rather stringent conditions on what is deemed a whistler wave, we argue that the true percentage of DF events that exhibit whistler emissions is somewhere in between the ratios for whistlers and waves. Also, in Figure 3 we see that the probability of finding a whistler wave at a DF is approximately independent of the tailward distance from Earth. Also, the amplitude of observed whistlers shows no discernible dependence on distance (not shown).

We also searched for whistler in all 2-minute intervals that Cluster spend in the tail box and found that the probability of detecting a whistler wave at a random position in the tail box is 1.5%, see Figure 4. The probability of finding a whistler wave at a DF is thus 20-40 times higher than for a random location in the magnetotail.

Almost all observed waves had a frequency less than 0.5 f_{ce}. The median frequency was about $0.16 f_{ce}$, with 25th and 75th percentiles lying at $0.09 f_{ce}$ and $0.29 f_{ce}$, respectively (not shown). This is consistent with the results presented by Zhang et al. [1999], who analyzed Geotail data consisting of approximately 1300 wave observations, though recorded throughout the magnetotail and not in any specific region or at any specific structure. The whistler wave in the event shown in Figure 1 is between $0.5 f_{ce}$ and f_{ce}, so it is not a typical event. Rather, we chose this particular event because it was observed by all four SC and had high resolution.

A histogram of the time difference from the DF to the whistler signal, Figure 5, shows that whistler observations are much more common after the DF than before, consistent with the waves being generated due to betatron acceleration.

5. Conclusions

Our investigation, which is the first to study the statistics of whistler waves specifically at dipolarization fronts, covers nine tail seasons of the Cluster data and utilizes all four Cluster spacecraft. We first search for DFs and find 1272 events, out of which 873 are unique. The DF events are then searched for whistler waves, and we find that whistlers are observed at approximately 30-60% of DF events. This is about 20-40 times more than the probability of finding a whistler wave at any random location in the tail box. The probability of finding whistlers is also several times higher directly at or after the DF than just before it, consistent with whistlers being a signature of betatron acceleration in the FPR. Thus, whistler waves may be used to detect dipolarization fronts when other data are not available, e.g. on planetary missions.

Whistler waves are known to heat electrons non-adiabatically and scatter them to low pitch angles, thereby contributing to electron precipitation into the inner magnetosphere. This fact, and that whistlers are very common at

DFs, means that whistlers are important in the dynamics of electrons in the magnetotail.

References

Asano, Y., Shinohara, I., Retinò, A., Daly, P. W., Kronberg, E. A., Takada, T., Nakamura, R., Khotyaintsev, Y. V., Vaivads, A., Nagai, T., Baumjohann, W., Fazakerley, A. N., Owen, C. J., Miyashita, Y., Lucek, E. A., and Rème, H.: Electron acceleration signatures in the magnetotail associated with substorms, Journal of Geophysical Research (Space Physics), 115, A05215, doi:10.1029/2009JA014587, 2010.

Balogh, A., Cargill, P. J., Carr, C. M., Dunlop, M. W., Horbury, T. S., Lucek, E. A., and Cluster FGM Investigator Team: Magnetic Field Observations on Cluster: an Overview of the First Results, in: Sheffield Space Plasma Meeting: Multipoint Measurements versus Theory, edited by Warmbein, B., vol. 492 of *ESA Special Publication*, p. 11, 2001.

Bortnik, J., Cutler, J. W., Dunson, C., and Bleier, T. E.: An automatic wave detection algorithm applied to Pc1 pulsations, Journal of Geophysical Research (Space Physics), 112, A04204, doi:10.1029/2006JA011900, 2007.

Cornilleau-Wehrlin, N., Chanteur, G., Perraut, S., Rezeau, L., Robert, P., Roux, A., de Villedary, C., Canu, P., Maksimovic, M., de Conchy, Y., Lacombe, D. H. C., Lefeuvre, F., Parrot, M., Pinçon, J. L., Décréau, P. M. E., Harvey, C. C., Louarn, P., Santolik, O., Alleyne, H. S. C., Roth, M., Chust, T., Le Contel, O., and Staff Team: First results obtained by the Cluster STAFF experiment, Annales Geophysicae, 21, 437–456, doi: 10.5194/angeo-21-437-2003, 2003.

Deng, X., Ashour-Abdalla, M., Zhou, M., Walker, R., El-Alaoui, M., Angelopoulos, V., Ergun, R. E., and Schriver, D.: Wave and particle characteristics of earthward electron injections associated with dipolarization fronts, Journal of Geophysical Research (Space Physics), 115, A09225, doi: 10.1029/2009JA015107, 2010.

Fu, H. S., Khotyaintsev, Y. V., André, M., and Vaivads, A.: Fermi and betatron acceleration of suprathermal electrons behind dipolarization fronts, *Geophys. Res. Lett.,* , 38, L16104, doi:10.1029/2011GL048528, 2011.

Fu, H. S., Khotyaintsev, Y. V., Vaivads, A., André, M., and Huang, S. Y.: Occurrence rate of earthward-propagating dipolarization fronts, *Geophys. Res. Lett.,* , 39, L10101, doi: 10.1029/2012GL051784, 2012a.

Fu, H. S., Khotyaintsev, Y. V., Vaivads, A., André, M., and Huang, S. Y.: Electric structure of dipolarization front at sub-proton scale, *Geophys. Res. Lett.,* , 39, L06105, doi: 10.1029/2012GL051274, 2012b.

Fu, H. S., Khotyaintsev, Y. V., Vaivads, A., André, M., Sergeev, V. A., Huang, S. Y., Kronberg, E. A., and Daly, P. W.: Pitch angle distribution of suprathermal electrons behind dipolarization fronts: A statistical overview, Journal of Geophysical Research (Space Physics), 117, A12221, doi: 10.1029/2012JA018141, 2012c.

Gustafsson, G., André, M., Carozzi, T., Eriksson, A. I., Fälthammar, C.-G., Grard, R., Holmgren, G., Holtet, J. A., Ivchenko, N., Karlsson, T., Khotyaintsev, Y., Klimov, S., Laakso, H., Lindqvist, P.-A., Lybekk, B., Marklund, G., Mozer, F., Mursula, K., Pedersen, A., Popielawska, B., Savin, S., Stasiewicz, K., Tanskanen, P., Vaivads, A., and Wahlund, J.-E.: First results of electric field and density observations by Cluster EFW based on initial months of operation, Annales Geophysicae, 19, 1219–1240, doi:10.5194/angeo-19-1219-2001, 2001.

Huang, S. Y., Zhou, M., Deng, X. H., Yuan, Z. G., Pang, Y., Wei, Q., Su, W., Li, H. M., and Wang, Q. Q.: Kinetic structure and wave properties associated with sharp dipolarization front observed by Cluster, Annales Geophysicae, 30, 97–107, doi:10.5194/angeo-30-97-2012, 2012.

Hwang, K.-J., Goldstein, M. L., Lee, E., and Pickett, J. S.: Cluster observations of multiple dipolarization fronts, Journal of Geophysical Research (Space Physics), 116, A00I32, doi: 10.1029/2010JA015742, 2011.

Khotyaintsev, Y. V., Cully, C. M., Vaivads, A., André, M., and Owen, C. J.: Plasma Jet Braking: Energy Dissipation and Nonadiabatic Electrons, Physical Review Letters, 106, 165001, doi:10.1103/PhysRevLett.106.165001, 2011.

Le Contel, O., Roux, A., Jacquey, C., Robert, P., Berthomier, M., Chust, T., Grison, B., Angelopoulos, V., Sibeck, D., Chaston, C. C., Cully, C. M., Ergun, B., Glassmeier, K.-H., Auster, U., McFadden, J., Carlson, C., Larson, D., Bonnell, J. W., Mende, S., Russell, C. T., Donovan, E., Mann, I., and Singer, H.: Quasi-parallel whistler mode waves observed by THEMIS during near-earth dipolarizations, Annales Geophysicae, 27, 2259–2275, doi:10.5194/angeo-27-2259-2009, 2009.

Liang, J., Ni, B., Cully, C. M., Donovan, E. F., Thorne, R. M., and Angelopoulos, V.: Electromagnetic ELF wave intensification associated with fast earthward flows in mid-tail plasma sheet, Annales Geophysicae, 30, 467–488, doi:10.5194/angeo-30-467-2012, 2012.

Owen, C. J., Fazakerley, A. N., Carter, P. J., Coates, A. J., Krauklis, I. C., Szita, S., Taylor, M. G. G. T., Travnicek, P., Watson, G., Wilson, R. J., Balogh, A., and Dunlop, M. W.: Cluster PEACE observations of electrons during magnetospheric flux transfer events, Annales Geophysicae, 19, 1509–1522, doi:10.5194/angeo-19-1509-2001, 2001.

Rème, H., Aoustin, C., Bosqued, J. M., Dandouras, I., Lavraud, B., Sauvaud, J. A., Barthe, A., Bouyssou, J., Camus, T., Coeur-Joly, O., Cros, A., Cuvilo, J., Ducay, F., Garbarowitz, Y., Medale, J. L., Penou, E., Perrier, H., Romefort, D., Rouzaud, J., Vallat, C., Alcaydé, D., Jacquey, C., Mazelle, C., D'Uston, C., Möbius, E., Kistler, L. M., Crocker, K., Granoff, M., Mouikis, C., Popecki, M., Vosbury, M., Klecker, B., Hovestadt, D., Kucharek, H., Kuenneth, E., Paschmann, G., Scholer, M., Sckopke, N., Seidenschwang, E., Carlson, C. W., Curtis, D. W., Ingraham, C., Lin, R. P., McFadden, J. P., Parks, G. K., Phan, T., Formisano, V., Amata, E., Bavassano-Cattaneo, M. B., Baldetti, P., Bruno, R., Chionchio, G., di Lellis, A., Marcucci, M. F., Pallocchia, G., Korth, A., Daly, P. W., Graeve, B., Rosenbauer, H., Vasyliunas, V., McCarthy, M., Wilber, M., Eliasson, L., Lundin, R., Olsen, S., Shelley, E. G., Fuselier, S., Ghielmetti, A. G., Lennartsson, W., Escoubet, C. P., Balsiger, H., Friedel, R., Cao, J.-B., Kovrazhkin, R. A., Papamastorakis, I., Pellat, R., Scudder, J., and Sonnerup, B.: First multispacecraft ion measurements in and near the Earth's magnetosphere with the identical Cluster ion spectrometry (CIS) experiment, Annales Geophysicae, 19, 1303–1354, doi:10.5194/angeo-19-1303-2001, 2001.

Runov, A., Angelopoulos, V., Sitnov, M. I., Sergeev, V. A., Bonnell, J., McFadden, J. P., Larson, D., Glassmeier, K.-H., and Auster, U.: THEMIS observations of an earthward-propagating dipolarization front, *Geophys. Res. Lett.,* , 36, L14106, doi:10.1029/2009GL038980, 2009.

Santolík, O.: Propagation analysis of STAFF-SA data with coherency tests, Lab. Phys. Chimie Environ./CNRS, lpce/nts/073a edn., 2000.

Sergeev, V., Angelopoulos, V., Apatenkov, S., Bonnell, J., Ergun, R., Nakamura, R., McFadden, J., Larson, D., and Runov, A.: Kinetic structure of the sharp injection/dipolarization front in the flow-braking region, *Geophys. Res. Lett.,* , 36, L21105, doi:10.1029/2009GL040658, 2009.

Sitnov, M. I., Swisdak, M., and Divin, A. V.: Dipolarization fronts as a signature of transient reconnection in the magnetotail, Journal of Geophysical Research (Space Physics), 114, A04202, doi:10.1029/2008JA013980, 2009.

Zhang, Y., Matsumoto, H., and Kojima, H.: Whistler mode waves in the magnetotail, *J. Geophys. Res.,* , 104, 28 633–28 644, doi: 10.1029/1999JA900301, 1999.

Zhou, M., Ashour-Abdalla, M., Deng, X., Schriver, D., El-Alaoui, M., and Pang, Y.: THEMIS observation of multiple dipolarization fronts and associated wave characteristics in the near-Earth magnetotail, *Geophys. Res. Lett.,* , 36, L20107, doi: 10.1029/2009GL040663, 2009.

H. Viberg, Swedish Institute of Space Physics, Uppsala, Sweden. (henrik.viberg@irfu.se)

Acknowledgments. We thank the ESA Cluster Active Archive for providing the data for this study. This research is supported by the Swedish National Space Board under grant number 135/11:2.